

# JGR Solid Earth

## RESEARCH ARTICLE

10.1029/2019JB018242

### Key Points:

- A GPS-buoy system has been designed, built, and tested to measure seafloor motion in shallow water
- GPS and buoy orientation measured by a digital compass enable the anchor position and effects of water motion to be accurately determined
- Daily repeatability of seafloor positioning is ~1–2 cm for horizontal components and better than 1 cm for the vertical component

### Supporting Information:

- Supporting Information S1
- Movie S1
- Movie S2
- Movie S3

### Correspondence to:

S. Xie,  
suruixie@mail.usf.edu

### Citation:

Xie, S., Law, J., Russell, R., Dixon, T. H., Lembke, C., Malservisi, R., et al (2019). Seafloor geodesy in shallow water with GPS on an anchored spar buoy. *Journal of Geophysical Research: Solid Earth*, 124, 12,116–12,140. <https://doi.org/10.1029/2019JB018242>









Received 20 JUN 2019

Accepted 10 OCT 2019

Accepted article online 24 OCT 2019

Published online 20 NOV 2019

## Seafloor Geodesy in Shallow Water With GPS on an Anchored Spar Buoy

Surui Xie<sup>1</sup> , Jason Law<sup>2</sup>, Randy Russell<sup>2</sup>, Timothy H. Dixon<sup>1</sup> , Chad Lembke<sup>2</sup>, Rocco Malservisi<sup>1</sup> , Mel Rodgers<sup>1</sup> , Giovanni Iannaccone<sup>3</sup> , Sergio Guardato<sup>3</sup> , David F. Naar<sup>2</sup> , Daniele Calore<sup>4</sup>, Nicola Fraticelli<sup>4</sup>, Jennifer Brizzolara<sup>2</sup>, John W. Gray<sup>2</sup>, Matt Hommeyer<sup>2</sup>, and Jing Chen<sup>2</sup> 

<sup>1</sup>School of Geosciences, University of South Florida, Tampa, Florida, USA, <sup>2</sup>College of Marine Science, University of South Florida, St. Petersburg, Florida, USA, <sup>3</sup>Istituto Nazionale di Geofisica e Vulcanologia, Osservatorio Vesuviano, Naples, Italy, <sup>4</sup>Hydra Solutions s.r.l., Casalserugo, Padova, Italy

**Abstract** Measuring seafloor motion in shallow coastal water is challenging due to strong and highly variable oceanographic effects. Such measurements are potentially useful for monitoring near-shore coastal subsidence, subsidence due to petroleum withdrawal, strain accumulation/release processes in subduction zones and submerged volcanoes, and certain freshwater applications, such as volcano deformation in caldera-hosted lakes. We have developed a seafloor geodesy system for this environment based on an anchored spar buoy topped by high-precision GPS. Orientation of the buoy is measured using a digital compass that provides heading, pitch, and roll information. The combined orientation and GPS tracking data are used to recover the three-dimensional position of the seafloor marker (anchor). A test system has been deployed in Tampa Bay, Florida, for over 1 year and has weathered several major storms without incident. Even in the presence of strong tidal currents which can deflect the top of the buoy several meters from vertical, daily repeatability in the corrected three-component position estimates for the anchor is 1–2 cm or better.

**Plain Language Summary** To measure seafloor motion in shallow water, we built a spar buoy and put a GPS antenna and a digital compass (three-dimensional orientation sensor) on top of it. The buoy rests on the sea bottom using a heavy concrete ballast. Rotation and other movements of the buoy are measured by the digital compass and GPS. Position of the ballast can be calculated based on these measurements. We tested the system in Tampa Bay, Florida, and found that it is able to measure motion of the anchor with an uncertainty of 1–2 cm or smaller.

## 1. Introduction

Space geodetic techniques such as global navigation satellite systems have achieved centimeter to millimeter precision and are now widely used to study Earth surface deformation (Bock & Melgar, 2016; Dixon, 1991; Herring et al., 2016; Li et al., 2013; Reilinger et al., 2006; Segall & Davis, 1997; Tregoning et al., 2009). However, precise application of these techniques is limited to land, whereas 71% of the Earth's surface, and most plate boundaries, are covered by water. There is a clear need for high-precision geodetic techniques that can work in the submarine environment (e.g., Bürgmann & Chadwell, 2014; Newman, 2011).

While several techniques for seafloor geodesy are available, they typically work best in the deeper ocean (>1-km water depth) where noise introduced by oceanographic effects is relatively low. The coastal ocean is a more challenging environment for measuring seafloor displacements, because its spatially and temporally variable oceanographic effects can be significant. Potential applications of a shallow seafloor geodetic system include monitoring of the following:

1. **Volcano deformation:** Some active volcanoes have monitoring areas partly covered by shallow water. Marine examples include Anak Krakatoa in Indonesia, Santorini caldera in Greece, and Campi Flegrei adjacent to the Bay of Naples, Italy. Freshwater examples include Yellowstone Lake in the United States, Lake Taupo in New Zealand, and Lago Nicaragua, which includes Ometepe Island and an active volcano, Concepción.

2. **Offshore oil fields:** Oil and gas field management can lead to significant uplift and/or subsidence. Accurate monitoring can help to assess reservoir performance and infrastructure integrity.
3. **Subduction zone strain accumulation and release processes:** Many subduction zones have extensive shallow continental shelves that could host shallow seafloor geodetic systems, potentially improving understanding and forecasting of large and great subduction zone earthquakes and tsunami waves.

Istituto Nazionale di Geofisica e Vulcanologia (INGV, the Italian Institute of Geophysics and Volcanology) has developed a GPS-tracked rigid buoy capable of measuring vertical seafloor displacement in water depths shallower than 150 m (De Martino et al., 2014; Iannaccone et al., 2018). Currently, they operate four such buoys close to Campi Flegrei, Italy. They use weekly averaged values of the vertical displacement component to estimate seafloor uplift associated with volcanic deformation, achieving performance that is comparable to on-land GPS. We have modified their design in order to determine both vertical and horizontal components of displacement and to reduce cost of the instrument. Here we describe the design, construction, and initial results of this system, and assess some potential applications.

## 2. Instrumentation and Test Site

### 2.1. System Design

Our system design is based on the successful Multiparametric Elastic-Beacon-Based Devices and Underwater Sensor Acquisition (MEDUSA) research and monitoring marine infrastructure used by INGV to monitor vertical deformation of the seafloor in the Gulf of Pozzuoli in southern Italy, adjacent to the Campi Flegrei volcanic area (De Martino et al., 2014; Iannaccone et al., 2018). Their infrastructure uses a global navigation satellite system receiver installed on top of each buoy, connected to the seafloor by either a rigid spar or, in deeper water (>40 m), a steel cable. Assuming that buoyancy maintains a near-vertical orientation, vertical displacement of the seafloor can be estimated by correcting the fraction of measured surface vertical motion induced by surface horizontal motion of the buoy using simple geometry (De Martino et al., 2014). We add heading/pitch/roll measurements to the system and perform a three-dimensional transformation to recover both horizontal and vertical components of the seafloor anchor (ballast) motion. Our system is called Shallow Underwater Buoy for Geodesy (SUBGEO) and can be used in coastal regions shallower than 40 m. It can be adapted to work in deeper water (<200 m) by adding a cable between the buoy and the ballast and performing additional orientation measurements.

The use of high-precision GPS systems for measuring seafloor movement requires both stability and a direct connection to the seafloor while also keeping the antenna and electronics safely above the waterline in all anticipated sea states. These requirements necessitate a design with a long spar connecting the GPS antenna to the seafloor, excessive net flotation for stability, and significant ballast to hold the system in place. Figure 1 a shows the system design. The above waterline section of the buoy consists of a superstructure (upper part) and access ladder. A GPS antenna is mounted on top at the center of the superstructure. A GPS receiver, a digital compass (Honeywell HMR3000), and associated electronics are installed in a fixed weather-proof enclosure rigidly connected to the superstructure, adjacent to exterior-mounted solar panels. This section of the buoy is designed to be lightweight and have a low cross-sectional area to minimize wind stress. However, there is sufficient space in the superstructure to incorporate additional instruments if required. Below the waterline, a polyurethane foam float is installed at a depth that ensures that it is continuously submerged regardless of sea state. Combined with increased displacement achieved by welding caps on the individual spar components, a net buoyancy of  $9 \times 10^3$  kg is provided to maintain the buoy in a nearly vertical position. At the bottom of the system, a 2.4 m  $\times$  2.4 m  $\times$  1.7 m concrete ballast reinforced by steel rebar is used as an anchor, attached to the buoy with a shackle. This concrete provides a ballast of  $\sim 1.3 \times 10^4$  kg when submerged in seawater. Therefore, when the buoyancy and ballast are combined, a net ballast (negative buoyancy) of more than  $4 \times 10^3$  kg is achieved.

### 2.2. Test Site

The test site is located on the bay side of Egmont Key within Tampa Bay, Florida, at a water depth of  $\sim 23$  m (Figure 1b). This section of the West Florida continental shelf is part of a broad, mostly submerged ancient carbonate platform with a thin layer of unconsolidated sediment over Miocene limestone (Berman et al., 2005; Doyle & Sparks, 1980; Evans et al., 1985; Hine, 1997, 2013; Hine et al., 2008). While the site is protected

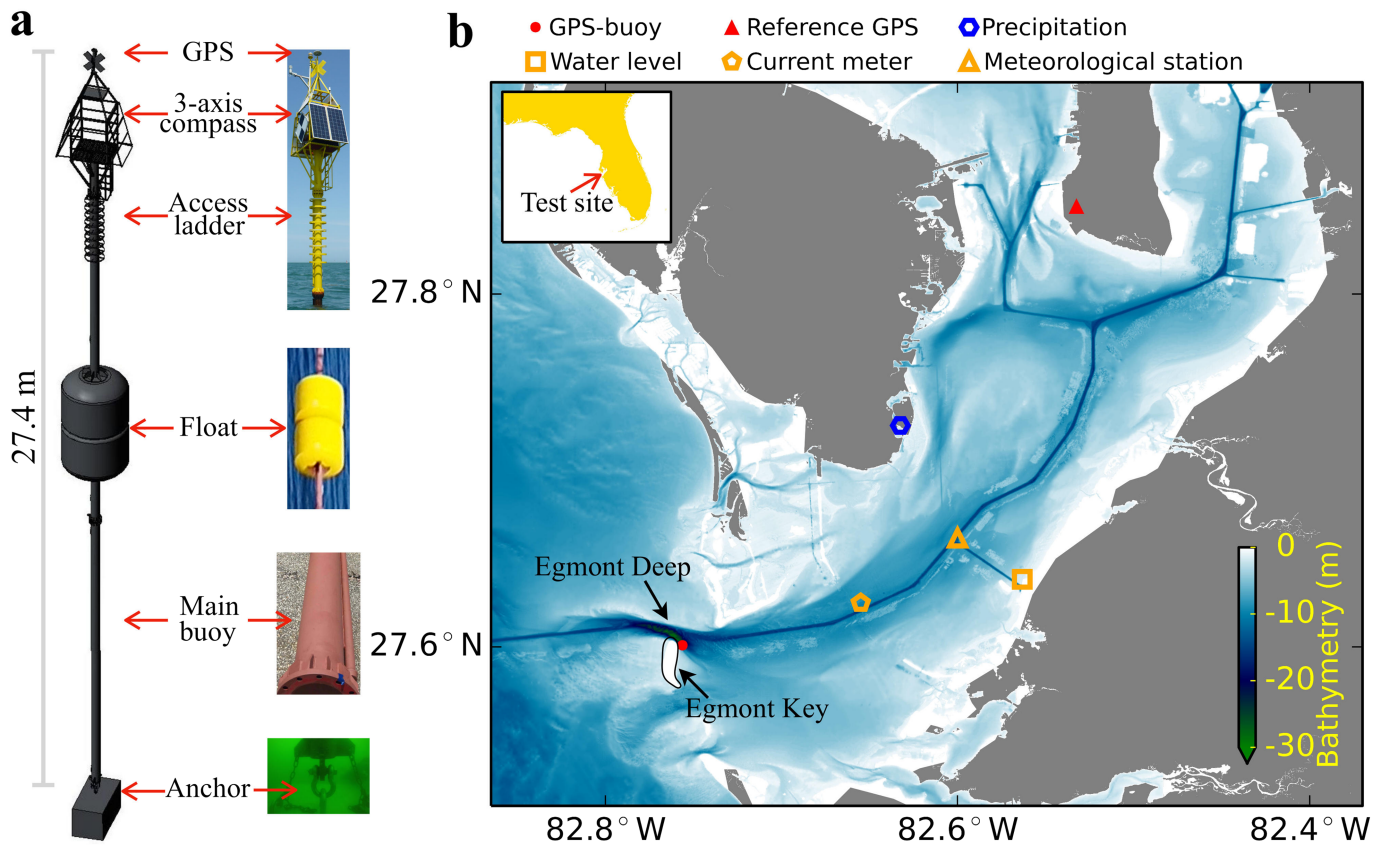


**Figure 1.** System design and test site. (a) System design. GPS is on top of the buoy, and associated electronics are mounted in a box below. The system is powered by solar-charged batteries. A float provides buoyancy, keeping the buoy close to vertical. The buoy is attached to a seafloor ballast through a large shackle. (b) Bathymetry of Tampa Bay, Florida. Markers show the test site and other nearby instruments. Note location of the GPS-buoy close to a tidal outflow channel.

from some of the wave energy from the Gulf of Mexico by Egmont Key, it experiences strong ebb and flood tidal currents (Berman et al., 2005, and references therein). Maximum current speeds in the channels adjacent to Egmont Key range from 1.8 m/s on the ebb tide to nearly 1.1 m/s on the flood tide (Stott & Davis, 2003). These currents cause correspondingly large deflections of the buoy from the vertical position and hence provide a rigorous test of our approach to horizontal motion corrections. The site is adjacent to the busy Egmont shipping channel (Berman et al., 2005; Gray, 2018) and occasionally experiences wake from passing ships.

The GPS-buoy deployment location is at the southern edge of a ~30-m deep known as Egmont Deep (previously Egmont Hole; Figure 1b). This deep and its connection to the Egmont Channel is analogous to the geologic term “gorge” or “throat”, which is a deep scoured bathymetric feature found at most barrier island inlets or passes (Berman et al., 2005, and references therein). The deepest part, the gorge, is formed and maintained by the strong tidal currents entering and exiting Tampa Bay. The formation of Egmont Deep is likely the result of a combination of karst and scour processes (Berman et al., 2005). The limestone bedrock here was subaerially exposed repeatedly during previous sea level low stands. Following the most recent ice age, sea level rose and flooded Tampa Bay, with subsequent sediment infilling of the deeps and channel scouring. Sediments adjacent to Egmont Deep consist primarily of coarse carbonate shell fragments and siliceous sand and silt (Berman et al., 2005; Brooks & Doyle, 1998; Doyle & Sparks, 1980; Ginsburg & James, 1974).

SCUBA observations made in December 2000 showed a seafloor nearly devoid of sediment, composed of smooth limestone with phosphatic nodules and small scour pits (Berman et al., 2005). Only large, rubble-sized limestone debris, oyster shells, and human trash were observed as unconsolidated materials in or near the deepest areas. Further north, a 30-m transect showed multicolored sponges. In April 2001,

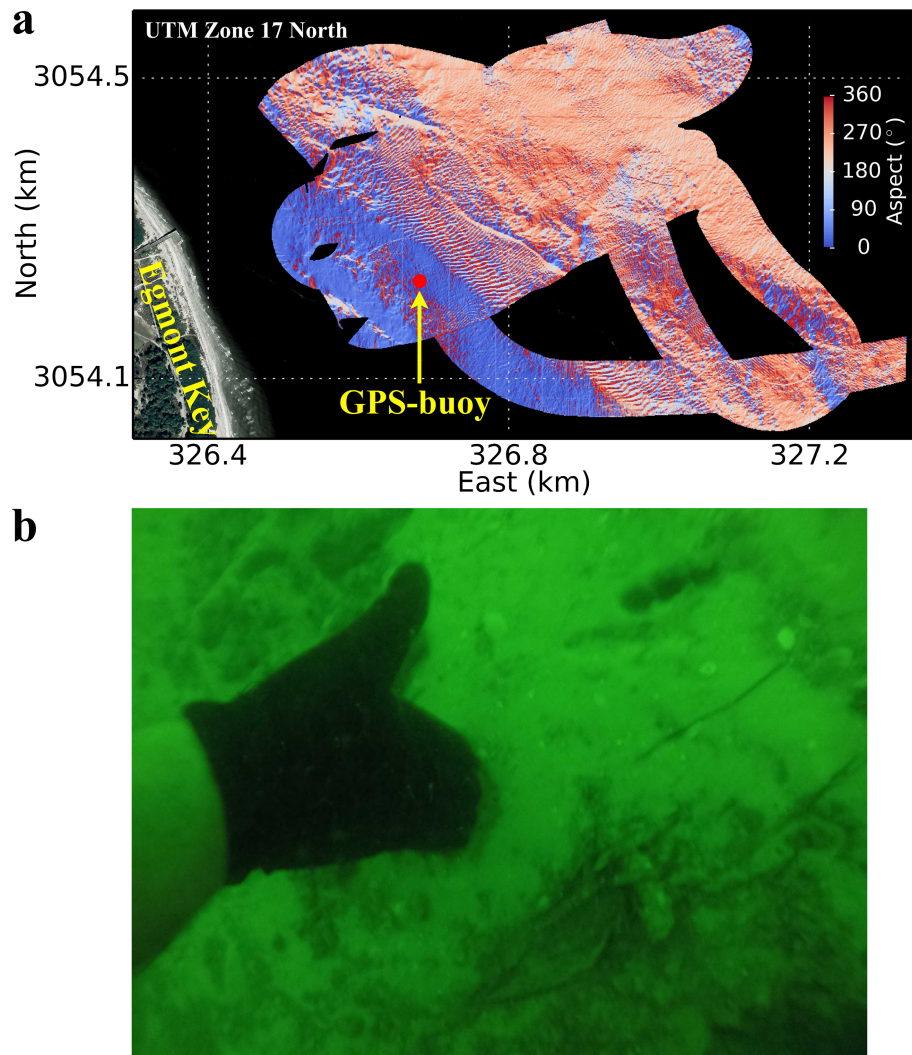


**Figure 2.** Bed characteristics of the test area. (a) Bed aspect map derived from multibeam sonar survey data. Aspect changes from light blue to red indicate subaqueous dunes. Aspect of 0° and 360° denote bed facing north. (b) Image of the seafloor at the test site during deployment. Diver's hand (in black neoprene glove) is penetrating several centimeters of soft sediment. Sediment here is primarily sand, with a thin muddy layer and some organisms above it. The unconsolidated sediment is at least 1.5-meter thick.

another SCUBA survey (while retrieving a deployed ADCP) showed a surface buried by ~0.5 m of shell fragments and coarse sediment, with previous rubble-sized debris no longer visible, possibly buried (Berman et al., 2005). These observations suggest a highly dynamic seafloor environment, presumably due to strong tidal currents, with any fine-grained sediment entering Egmont Deep periodically transported out of the area. The buoy location is immediately southeast of the deepest, high velocity part of the channel and, at the present time, contains some reworked sediments, subaqueous dunes, and smaller sedimentary bedforms (Figure 2a). Diver observations on 1 October 2019 showed the presence of unconsolidated sandy sediment at least 1.5-m thick, based on the length of rebar driven into the sediment.

Berman et al. (2005) compare bathymetry collected using the same multibeam system (Kongsberg Simrad EM3000 300 kHz system) from surveys made in 1999 and 2001. They observed large dunes near the study site with 2-m vertical relief, an average slope of 6°, and average wavelength of 150 m, with smaller superimposed dunes with typical relief of 0.3 m, wavelength of 5–9 m, and length of ~50–150 m. At the study area, smaller dunes are observed with some slopes up to ~10°. In April 2018, multibeam data from a Reson SeaBat



**Figure 3.** Deployment of assembled mooring. Main winch line is attached to the anchor, while the auxiliary line with two-point sling supports the spar section. Inserts show design of the ballast, note indented bottom.

T50-R dual-head 200–400-kHz system (run at 400 kHz) were collected in the study area. These data also show the presence of numerous small subaqueous dunes near the buoy location (Figure 2).

### 2.3. Deployment

As detailed in the section 2.1, the system's high-resolution GPS application demands a moored structure with net flotation and ballast mass to provide sufficient stability while also keeping the antenna and electronics above the waterline in all sea states. The system's spar length of  $\sim 30$  m and combined in air weight of  $\sim 2.7 \times 10^4$  kg make the deployment logistically complicated. For this reason, Orion Marine Group of Tampa was contracted to perform the deployment using a 46-m barge equipped with a 250-ton ( $2.5 \times 10^5$  kg) crane.

While the system is designed to be deployable in two stages, allowing a fully instrumented tower to be bolted onto the uppermost spar flange after it is in place, an alternate plan was used for our deployment. Strong tidal currents at the mouth of Tampa Bay introduced potential issues of aligning the two flanges near the waterline in a two-stage deployment. For this reason, the system was deployed fully assembled except for the electronics. The electronics were then installed via small boat after the buoy was in place.

The use of a large crane with an auxiliary line makes a single-stage deployment possible. As shown in Figure 3, the anchor is lifted via the main winch line, while an auxiliary line supports the spar section at two lifting points with a custom sling. This method minimizes the time required for the crane and barge to be on site. The entire deployment including a 3-hour transit was accomplished in approximately 6 hr, with an additional 6 hr required for installation of power and electronics components. The deployment was executed successfully on 23 August 2018, with data transmitting 6 hr after the anchor was placed on the bottom. The detail found in the supporting information in Figure S1 shows the above waterline section of the system.

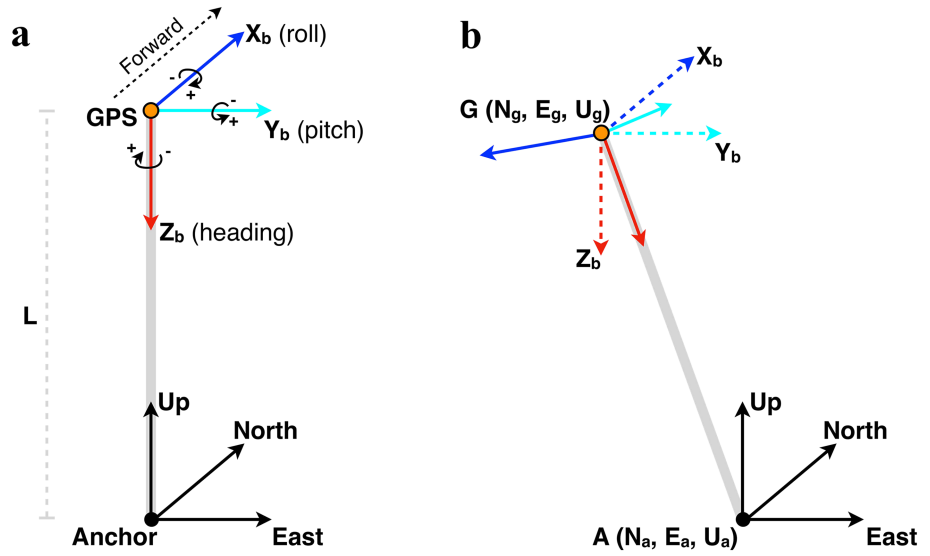


**Figure 4.** Observation geometry of the system. (a) State of the system when the buoy (represented by thick gray line) is vertical and three axes of the digital compass are at initial orientations (heading/pitch/roll measurements are all zero). Signs of these measurements follow the right-hand rule. (b) State of the system when GPS and digital compass modules are perturbed from initial positions. Solid color arrows show perturbed orientations of heading/pitch/roll axes. Dashed color arrows show reference directions.

### 3. Data Analysis

GPS data are collected at 15-second intervals. Heading, pitch, and roll are measured by the digital compass every 5 sec with  $0.1^\circ$  resolution. All data are downloaded through a Freewave radio link  $\sim 2.5$ -km away from the buoy. Here we report data obtained between 23 August 2018 and 24 August 2019 (Dixon et al., 2019). Data gaps during this period occurred  $<0.01\%$  of the time.

#### 3.1. Three-Dimensional Transformation to Estimate Anchor Position

The ballast serves as a seafloor marker, and its displacement is used as a proxy for seafloor motion. Because of its large mass, it should be relatively stable except during extreme sea states or weather events. Figure 4 shows the system geometry. Anchor position ( $N_a$ ,  $E_a$ , and  $U_a$ ) can be calculated using

$$\begin{bmatrix} N_a \\ E_a \\ U_a \end{bmatrix} = \begin{bmatrix} N_g \\ E_g \\ U_g \end{bmatrix} + \begin{bmatrix} N_{ag} \\ E_{ag} \\ -U_{ag} \end{bmatrix}, \quad (1)$$

where  $N_g$ ,  $E_g$ , and  $U_g$  are north/east/up components of the GPS position and  $N_{ag}$ ,  $E_{ag}$ , and  $U_{ag}$  represent anchor coordinates defined in a local Cartesian coordinate system  $G$ - $X_b$  $Y_b$  $Z_b$  whose origin is at the GPS antenna phase center and whose three axes point to geographic north/east/down (shown in Figure 4a by blue-, cyan-, and red-colored arrows).  $N_{ag}$ ,  $E_{ag}$ , and  $U_{ag}$  can be calculated using a three-axis rotation:

$$\begin{bmatrix} N_{ag} \\ E_{ag} \\ U_{ag} \end{bmatrix} = R_z(-\alpha)R_y(-\beta)R_x(-\gamma) \begin{bmatrix} 0 \\ 0 \\ L \end{bmatrix}, \quad (2)$$

where  $L$  is the length of the buoy (defined as length from the GPS antenna phase center to the pivot point of the anchor-shackle system).  $\alpha$ ,  $\beta$ , and  $\gamma$  are measured heading, pitch, and roll angles of the buoy. Their signs are defined by the right-hand rule (Figure 4a). The three rotation matrices in equation (2) are calculated by the following:

$$R_x(-\gamma) = \begin{bmatrix} 1 & 0 & 0 \\ 0 & \cos(\gamma) & -\sin(\gamma) \\ 0 & \sin(\gamma) & \cos(\gamma) \end{bmatrix}. \quad (3)$$

$$R_y(-\beta) = \begin{bmatrix} \cos(\beta) & 0 & \sin(\beta) \\ 0 & 1 & 0 \\ -\sin(\beta) & 0 & \cos(\beta) \end{bmatrix}. \quad (4)$$

$$R_z(-\alpha) = \begin{bmatrix} \cos(\alpha) & -\sin(\alpha) & 0 \\ \sin(\alpha) & \cos(\alpha) & 0 \\ 0 & 0 & 1 \end{bmatrix}. \quad (5)$$

Based on equations (1–5), for a given time, if GPS position and heading/pitch/roll of the superstructure are measured, position of the anchor can be estimated. Note that heading in these equations is relative to geographic north; therefore, a correction for magnetic declination is needed.

### 3.2. GPS Data Processing

Most of our GPS data are processed using the TRACK v1.30 kinematic processing software (Chen, 1998; Herring et al., 2018). We also processed some data using the free online GPS processing tool of the Canadian Spatial Reference System (CSRS) provided by the Canadian Geodetic Survey (<https://webapp.geod.nrcan.gc.ca/geod/tools-outils/ppp.php?locale=en>, last access on 23 September 2019) for comparison. For TRACK processing, a stationary GPS site 35 km away from the buoy is used as reference station (red triangle in Figure 1b). Our kinematic site positions, representing the instantaneous position of the phase center of the GPS on top of the buoy, are estimated in long baseline mode, with motion modeled as a random walk. We set allowable changes in position for all three components to be 1 m/sec, approximately the same as the speed of a typical tidal current in the bay. A cutoff angle of 15° is used to reduce the influence of multipath. GPS position is estimated at 15-second intervals, the sampling rate of the GPS observations.

Our GPS raw data are written as daily files. To minimize potential jumps at the boundaries of each day due to smoothing gaps, we use 30 hr of data centered on the middle of each day to form session files. For a few known jumps (caused by anchor slip immediately after deployment, hurricanes, or periods of other extreme weather), we omit data within 2 hr of the visually inspected large jumps and do not allow sessions to span the jumps. After finishing each processing session, we remove position estimates the day before and after (data during 21:00–24:00 in the previous day and 00:00–03:00 in the next day), and epochs with any ambiguities unfixed to integer values are deleted. Typical formal error estimates for a single epoch are 1.5–2.0 cm for the horizontal components and 4–5 cm for the vertical component. Note that TRACK uses differential phase measurements to estimate GPS positions; thus, observations from both the kinematic and reference stations are required. Data gaps (mainly due to data gaps in the reference station) lead to solution gaps but only account for a small fraction of the resulting displacement time series.

Black dots in Figure 5 show the kinematic GPS positions processed using TRACK. Red dots show solutions by CSRS for comparison. CSRS uses a precise point positioning (PPP) strategy and does not require reference stations. Solutions from these two processing streams show good agreement (Figure 5), with relatively large differences mostly occurring when tidal current speed is high and tilt of the antenna is largest. These points are flagged as outliers (below) and not used for anchor position estimates. Due to the advantage of not requiring a reference station, there are fewer gaps in the CSRS solutions. However, currently the online CSRS-PPP tool needs individual data files to be uploaded manually. We therefore use the CSRS-PPP tool to fill gaps in TRACK results caused by outages at the reference station.

### 3.3. Magnetic Correction for Digital Compass

The digital compass module consists of three magneto-resistive sensors oriented in orthogonal directions plus a two-axis fluid tilt sensor, creating tilt-compensated heading, pitch, and roll data. The tilt sensor works best when kept near level (HMR3000 data sheet from Honeywell International Inc., 2019). Although the digital compass can update continuous data with a frequency up to 8 Hz, fast jarring of the sensor degrades pitch/roll measurements and affects tilt compensated headings because not all the fluid can immediately

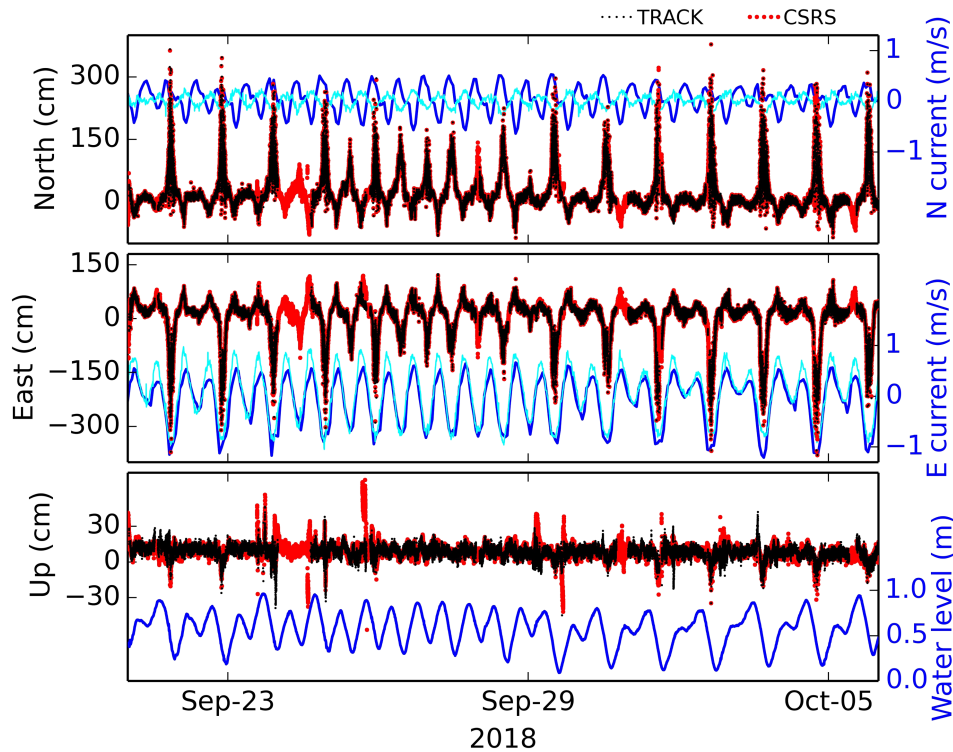


**Figure 5.** 15 days of GPS and selected oceanographic data. Black dots show processed GPS positions using TRACK kinematic processing software (Chen, 1998; Herring et al., 2018). Red dots are results processed using the online tool of the Canadian Spatial Reference System (CSRS) Precise Point Positioning (PPP). Except for a few outliers, solutions from these two software programs match well. Data gaps in TRACK solutions are mainly due to data gaps in the on-land reference station. Cyan curves in the upper two panels show surface tidal current speeds from the nearby current meter shown in Figure 1b; blue curves show the Tampa Bay Coastal Ocean Model (TBCOM) hindcast surface current speeds at the GPS-buoy location (Chen et al., 2018, 2019). GPS motion is positively correlated with current velocity (the linear correlation coefficient between GPS displacement and the modeled current speed is 0.56 for the north component and 0.80 for the east component).

return to the bottom of the tilt sensor's glass ampoule (HMR3000 data sheet from Honeywell International Inc., 2019). Therefore, heading/pitch/roll measurements are less accurate when pitch or roll is large. Figure 6 shows outputs from the digital compass. During the observation period, pitch/roll measurements are all within  $\pm 20^\circ$  and mostly  $\pm 5^\circ$ . With this range, the nominal repeatability for a heading measurement should be  $\pm 0.3^\circ$ , while pitch and roll measurements should be  $\pm 0.2^\circ$  according to the manufacturer (HMR3000 data sheet from Honeywell International Inc., 2019). We assume that within a short period (e.g.,  $< 1$  min in our case), the buoy moves smoothly and uses a 1-minute Gaussian filter to smooth heading/pitch/roll measurements. Red lines in Figure 6 show smoothed data. This smoothing significantly reduces the scatter of heading/pitch/roll observations (Figure 7b). We corrected magnetic declination using the World Magnetic Model (WMM2015v2), which is about  $-5.4^\circ$  during the observation period at the GPS-buoy location. Thus, all heading data presented here are relative to geographic north.

While pitch/roll measurements are controlled by the force of gravity on fluid in the tilt sensor, heading measurements represent changes of buoy orientation and are sensitive to the local magnetic environment and its changes. Therefore, variation of local magnetic environment (e.g., caused by orientation of the superstructure) can induce offset in the heading measurements. Thus, heading output from the digital compass may be offset from the true heading direction. Leaving this offset uncorrected would impart a significant systematic error to our tilt correction, affecting the precision and accuracy of the horizontal component estimates for the ballast. In order to avoid this bias, we applied the following corrections.

We assume that for a short period (e.g., 1 day), offset in the heading measurement is constant and the anchor is stationary or moves linearly. Offset of the heading measurement is estimated by minimizing the weighted one standard deviation (SD) of anchor position residuals. As mentioned above, outputs from the digital compass are less accurate when the tilt angle is large. GPS solutions are also noisy when pitch or roll is large (see



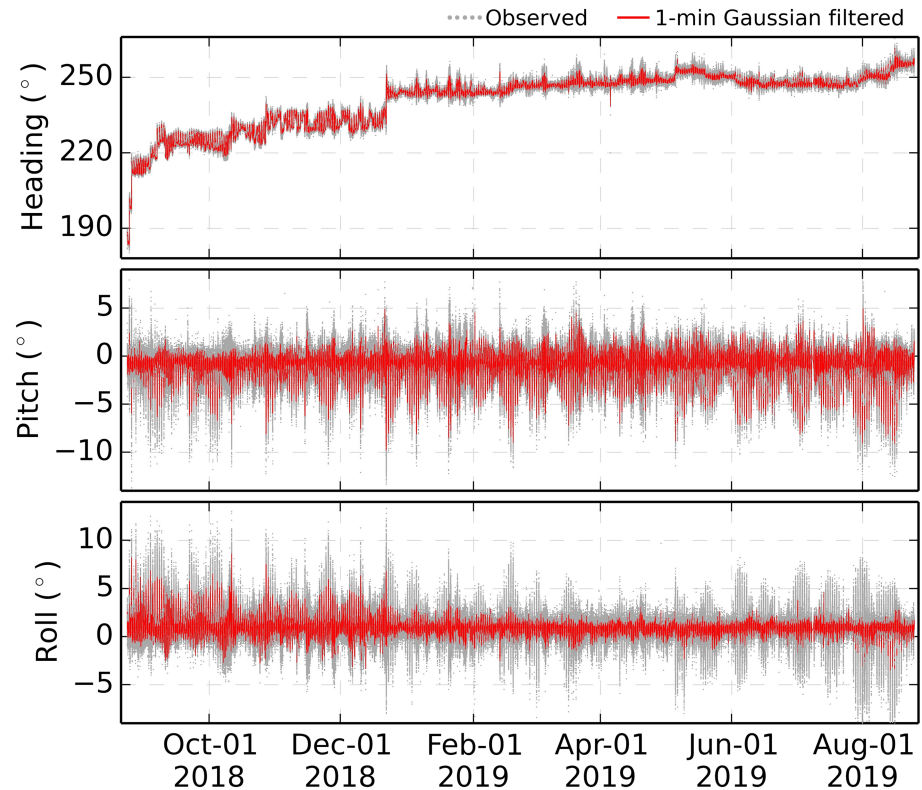


**Figure 6.** Heading/pitch/roll measurements over the sampled time period. Gray dots are observed time series. Magnetic declination in heading measurements is corrected using the World Magnetic Model (WMM2015v2, <https://www.ngdc.noaa.gov/geomag/WMM/soft.shtml#downloads>). Red lines show 1-minute (13 data point window) Gaussian filtered time series. See Figure 7b for an example data in 1 day.

red dots in Figure 7a, corresponding to periods of high-speed tidal currents). We therefore mask out data when either pitch or roll exceeds  $2^\circ$  in any direction. A grid search with a step width of  $0.1^\circ$  (resolution of the digital compass measurements) is used to estimate the heading offset. Black dots in Figure 7c show anchor position time series for a typical day with estimated heading offset corrected and show considerable improvement. Figure 8 shows anchor position for the same day in a plan view. For comparison, blue dots in Figure 7c shows position time series assuming no instrumental offset for the digital compass. Note that we apply a modified Z-score method (Iglewicz & Hoaglin, 1993) to detect outliers in anchor position estimates for each session. For a given period, Z-score of the  $i$ -th anchor position estimate  $x_i$  is

$$Z_i = 0.6745|x_i - \bar{x}|/\text{MAD}, \quad (6)$$

where  $\bar{x}$  is the median value of all position estimates during the period and MAD denotes the median absolute deviation

$$\text{MAD} = \text{median}(|x - \bar{x}|), \quad (7)$$

with  $x$  denoting a list of all position estimates during the period. We set a threshold Z-score of 3.5, as recommended by Iglewicz and Hoaglin (1993). Any of the north/east/up components with Z-scores exceeding this value are considered outliers and removed. Orange dots in Figure 7c show detected outliers for the example day.

The pitch/roll measurements should not have significant offsets since they use a gravitational reference. We also tested possible corrections to these measurements using the same method as for heading offset, but the best estimates are mostly within  $\pm 0.2^\circ$  of the measured values (Figure 7d shows an example). Thus, we

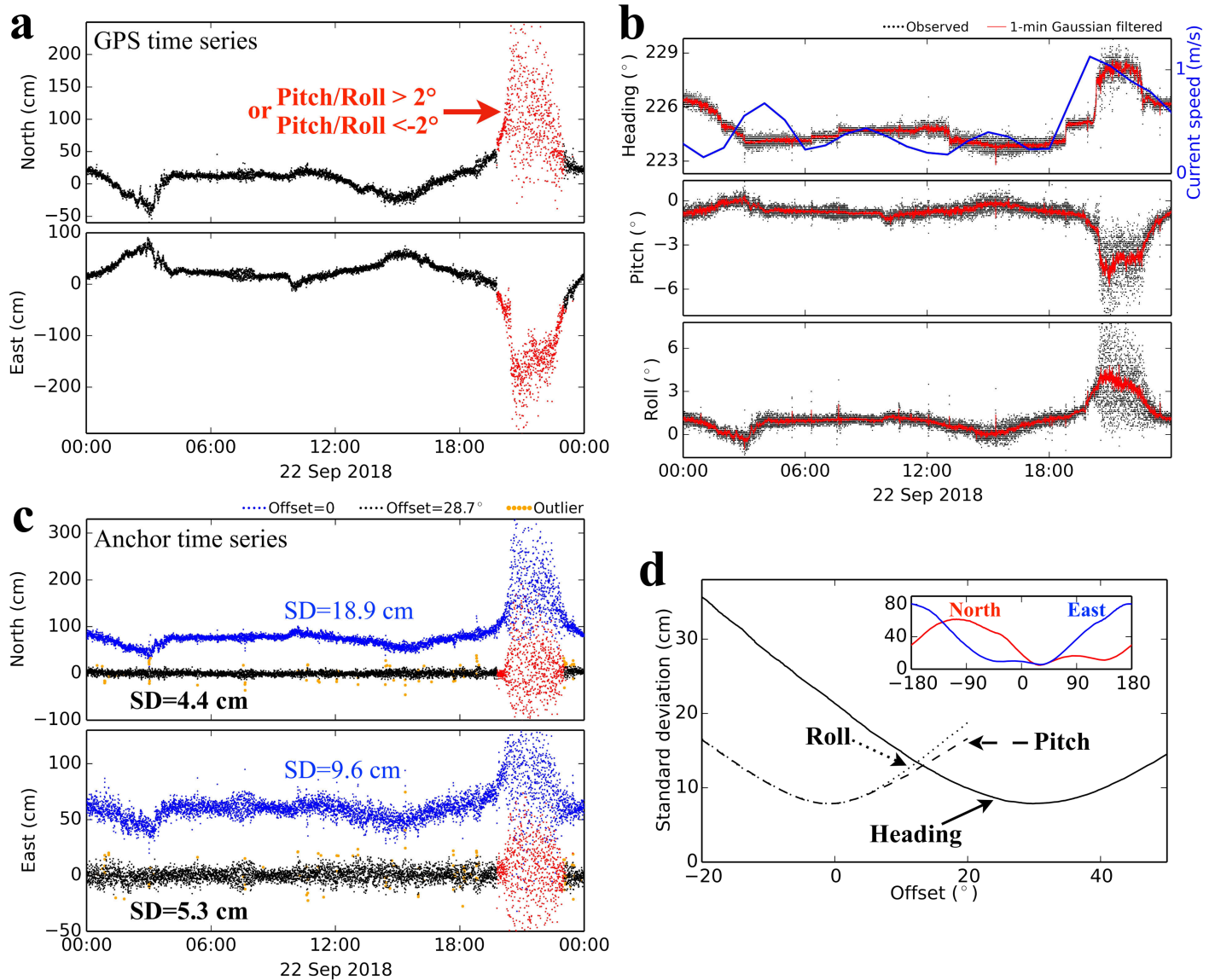


**Figure 7.** Heading offset and anchor position estimates for 22 September 2018. (a) North/east components of GPS time series, red marks data when pitch or roll measurements are  $>2^\circ$  or  $<-2^\circ$ . (b) Heading/pitch/roll measurements. Note due to the  $0.1^\circ$  resolution of digital compass, these observations have small steps changes around the Gaussian filtered time series. Large pitch/roll are observed when current speed is high. (c) Blue dots show calculated positions using heading data corrected for magnetic declination. Black dots are calculated positions by adding an offset to heading data (magnetic declination corrected) that minimizes scatter of one day anchor positions. Red corresponds to pitch or roll exceeding  $2^\circ$ , orange dots are detected outliers. Weighted one standard deviation (SD) for north and east components are shown. Note that different offsets in heading do not affect estimates of vertical component, thus we do not show vertical positions here. (d) Weighted one standard deviation (root of the sum square of north and east components) when adding different offsets to digital compass measurements for 22 September 2018. Inset shows for a wider range of heading offset, units of X and Y axes are the same as (d).

assume no offset in pitch/roll measurements in the following analysis. Possible residual errors related to measurement of heading/pitch/roll are analyzed in section 4.

The black line in Figure 9 shows the estimated heading offset (modeled as a constant offset for each session) during the entire observation period. Except for days with flagged jumps, they are shown with daily increments. Note that there are considerable changes in the first few months, some of which are caused by rapid reorientation of the buoy as it settled to a stable position, as well as a step change associated with a major unnamed storm around 20 Dec 2018.

We tested the validity of our heading correction technique using an independent estimate based on optical image analysis. While such an analysis would not be possible in most offshore locations, it is useful here as a

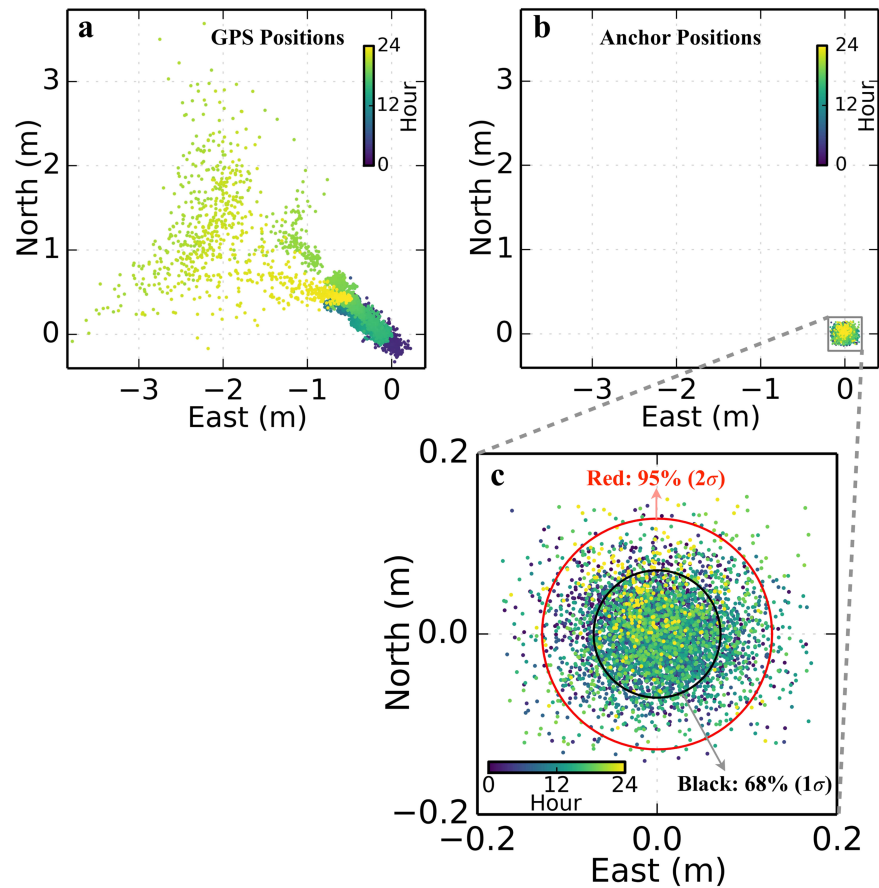
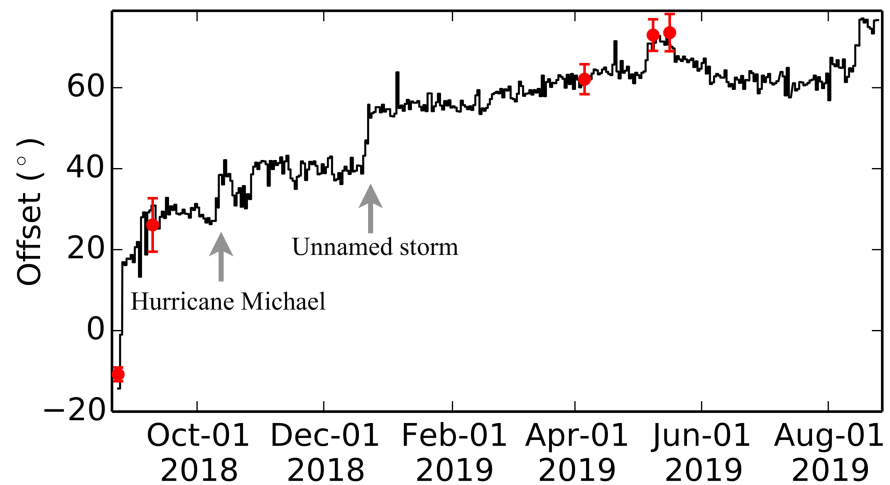


**Figure 8.** GPS and estimated anchor positions for a single day (22 September 2018). (a) GPS position time series. (b) Estimated anchor positions. Gray box outlines an area shown in (c). (c) Black and red circles mark 68% (7.1 cm) and 95% (12.8 cm) of the distances from the daily median position. Note that (a) and (b) are of the same spatial scale. (c) is a close-up of the outlined box in (b).

check on the least squares estimation procedure described above. The image analysis uses an inverse perspective transformation (done with OpenCV-Python module) of photographic images taken from a boat or an unoccupied aerial vehicle that includes the buoy and known points on nearby Egmont Key (Figure S1). The thin bars of the superstructure are parallel or perpendicular to the forward direction (origin direction for heading measurements, shown by dashed arrow in Figure 4a) of the digital compass. Their orientations are used to construct parallel lines that intersect at a vanishing point (estimated using least squares) in a camera perspective projection (Figure S2b). The buoy water surface contact and the vanishing point thus form a line that is parallel to the forward direction of the digital compass. The orientation of its projection can be estimated using the georeferenced image. Using this method and multiple images taken during each site visit, variation of the offset in heading measurements can be estimated (Figures S2–S5). Red dots and error bars in Figure 9 represent the mean and two standard derivation of estimates for each visit. This approach yields results that are consistent with the heading offset estimation procedure described above using the least squares. Large changes in heading offset occurred in the first month after deployment, as well as several days of extreme weather.

### 3.4. Seafloor Marker Positioning

We apply the estimated heading offsets and use equations (1) to (5) to recover anchor positions for the entire period. Figure 10a shows the full period of the observed GPS time series (top of buoy). Figure 10 b shows time series for the corresponding anchor position, with 15-second intervals in dark gray and daily median time series in red. We use the median position of each day as the best estimate and the weighted one SD as a measure of uncertainty ( $1\sigma$ ) for each day. Daily solutions and uncertainties are shown in



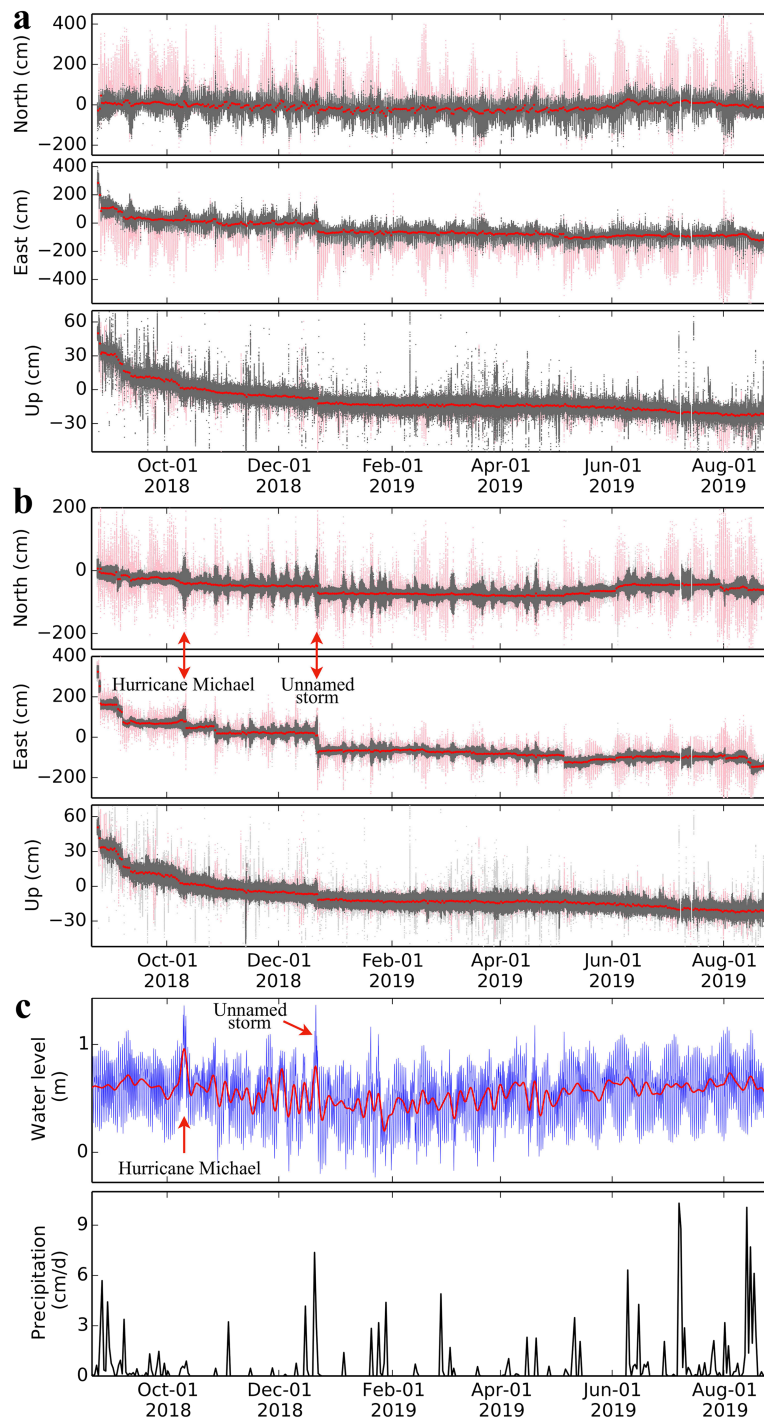
**Figure 9.** Heading offset variations. Black line shows heading offset (compass forward axis azimuth direction minus compass measured heading) estimates by minimizing daily anchor displacements (see an example in Figure 7c), shown with daily increments. Red dots with error bars ( $2\sigma$ ) are estimates using inverse perspective transformation method shown in the supporting information in Figures S2–S5.

Figure 11a. During the first month after deployment, the system experienced rapid horizontal motion of several meters and vertical subsidence of  $\sim 0.5$  m. In the next 7 months, the anchor was relatively stable except for short perturbations associated with extreme weather. Large perturbations occurred due to passage of Hurricane Michael (around 10 October 2018) or during an extreme weather event with heavy precipitation (around 20 December 2018; Figure 10c). During the following summer (June, July, and August 2019), there were frequent extreme weather events (see precipitation data in Figure 10c), causing significant anchor motion. Several other large displacements occurred during periods of exceptionally high current periods (Figure S6). In general, long-term displacement of the anchor mimics long-term displacement of the GPS (Figures 10a and 10b), since the anchor constrains GPS position by a rigid connection.

To assess the repeatability of seafloor marker positioning using our GPS-buoy system, we analyze time series for the  $\sim 5$ -month period from 25 December 2018 to 1 May 2019 (Figure 11b) when no major storms affected the area. The displacements are modeled as simple functions, and then the SD is computed to assess repeatability. The vertical position of the anchor is modeled as exponentially decreasing subsidence. The horizontal position components of the anchor are assumed to behave linearly with near-zero velocity, except for several discrete steps. Displacements are modeled following Larson et al. (2004):

$$x(t_i) = A + Be^{Ct_i} + \sum_{k=1}^n \frac{D_k}{2} \left( \tanh \frac{t_i - T_k}{\tau_k} - 1 \right), \quad (8)$$

where  $x(t_i)$  is the anchor position estimate at time  $t_i$ .  $A$ ,  $B$ ,  $C$ , and  $D_k$  are parameters to be estimated.  $D_k$ ,  $T_k$ , and  $\tau_k$  are the displacement, middle time, and duration half width of the  $k$ -th transient events, respectively. Horizontal displacements occurred in three discrete events (Table 1). We set  $B = 0$  for horizontal components assuming settling-related displacement is trivial in horizontal displacements during the selected period, and we set  $D_k = 0$  for the vertical component assuming transient event-related displacement is insignificant during the selected period. We use visually inspected values for  $T_k$  and  $\tau_k$ . Red lines in Figure 11a mark the selected period shown in Figure 11b. Dashed pink lines in Figure 11a mark selected transient events modeled in equation (8), chosen by visual inspection. Red curves in Figure 11b show best-fitting curves to the daily time series. Weighted one SD of the residual time series for each component is used as a measure of repeatability. For horizontal components, the SD is about 1–2 cm and is larger in the east-west direction, where tidal current amplitude is much larger than in the north-south direction (Figure 5). For the vertical component, the SD is less than 1 cm. The horizontal component repeatability of our GPS-buoy system is about 10 times larger than a nearby land site (1.4 mm), while the vertical component repeatability is at a similar level (4.8 mm; Figure S7).



**Figure 10.** Top of buoy position (a), anchor position (b), and selected environmental data (c). (a) Dark gray dots show GPS positions when both pitch and roll measurements are between  $-2^\circ$  and  $2^\circ$ . Pink dots are when pitch or roll exceed  $\pm 2^\circ$ . Red dots are daily medians from the data shown by dark gray dots. (b) Dark gray dots using data when both pitch and roll measurements are between  $-2^\circ$  and  $2^\circ$ ; pink dots correspond to pink dots in (a); light gray dots are detected outliers. Red are daily medians from the data shown by dark gray dots. (c) Water level and precipitation records near the test site. Blue curve shows observed water level (location of tide gauge shown in Figure 1b). Red curve shows 0.2 cycle-per-day low-frequency pass-filtered water level. In the lower panel, precipitation data are daily accumulated records (location of station shown in Figure 1b).

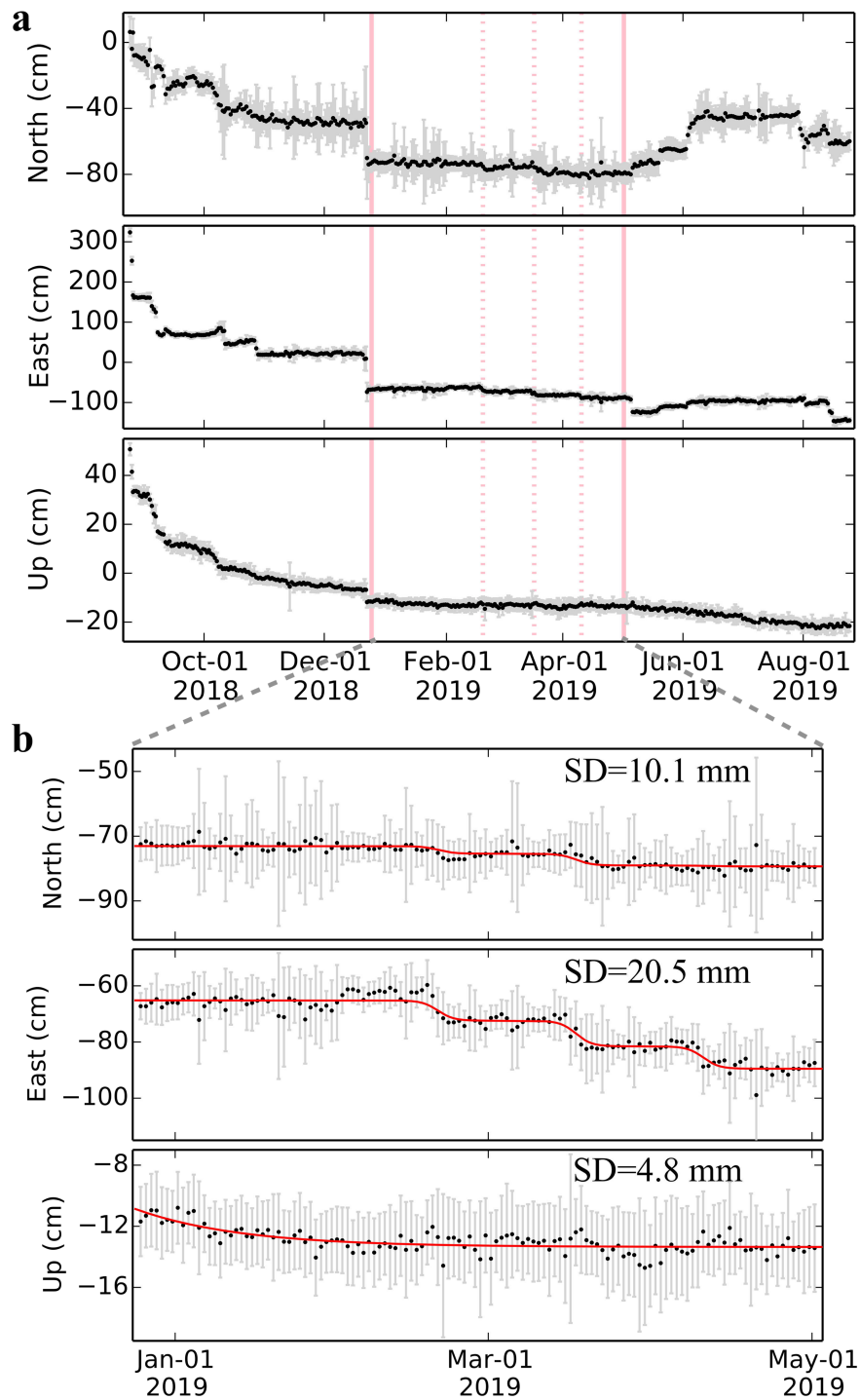


**Figure 11.** Anchor displacement estimates. Black dots are session medians (mostly daily except for interrupted sessions), with  $1\sigma$  uncertainties shown by light gray color bars. (a) Time series of the entire analyzed period. Solid pink lines mark the period shown in (b). Dashed pink lines mark three slip events modeled in (b). (b) Time series for the period 25 December 2018 to 1 May 2019. Red curves are best-fitting curves using equation (8). Weighted one standard deviation (SD) of model residuals during this ~5-month period is calculated to assess repeatability.

**Table 1**  
*Modeled Horizontal Displacements During Three Discrete Events*

Time (DD-MM-YYYY)	North disp. (cm)	East disp. (cm)
19-02-2019	$-2.4 \pm 0.4$	$-7.2 \pm 0.6$
17-03-2019	$-3.6 \pm 0.4$	$-9.1 \pm 0.8$
10-04-2019	$-0.3 \pm 0.4$	$-8.0 \pm 0.8$

## 4. Discussion

### 4.1. Error Analysis

Error sources for the anchor position estimates consist of two types: (1) GPS measurement and processing errors and (2) three-dimensional transformation errors due to input parameter errors, that is, errors in  $N_{ag}$ ,  $E_{ag}$ , and  $U_{ag}$  using equation (2). While we apply relatively loose constraints on the GPS data processing (we model GPS motion as a random walk and

allow all three components to move up to 1 m/sec), solutions from TRACK and CSRS show good consistency. The formal errors in TRACK outputs are typically 1.5–2.0 cm for horizontal components and 4–5 cm for vertical components, comparable to other kinematic GPS applications (e.g., Chen, 1998 ; Davis et al., 2014; Watson et al., 2008). Here we analyze errors associated with three-dimensional transformation in equation (2), which are likely to be the dominant error source.

In equation (2), we assumed that the GPS and the anchor are perfectly on a line that crosses the long axis of a rigid buoy; therefore the anchor coordinates in a reference frame defined by the GPS and three rotation axes ( $G-X_b Y_b Z_b$  in Figure 4) were (0, 0,  $L$ ). In reality, either GPS or the pivot of the shackle may be located at a slightly biased position, and  $L$  contains measurement error. That is, the anchor coordinates in  $G-X_b Y_b Z_b$  are  $p$ ,  $q$ , and  $L$ , where  $p$ ,  $q$ , and  $L$  represent anchor point coordinates along the roll/pitch/heading axes of the digital compass. Thus, there are six parameters ( $p$ ,  $q$ ,  $L$ ,  $\alpha$ ,  $\beta$ , and  $\gamma$ ) on the right side of equation (2). Errors in these parameters will be propagated to  $N_{ag}$ ,  $E_{ag}$ , and  $U_{ag}$ . Assuming the six parameters are independent, we rewrite equation (2) in equation (A1) and take the partial derivatives of  $N_{ag}$ ,  $E_{ag}$ , and  $U_{ag}$  in equations (A2–A4). Some of the items can be ignored in the total error budget, some will counteract each other, and some will only cause a systematic error for all position estimates that will not affect displacement estimates. We ignore terms where more than two small values multiply together. For example,  $\cos(\alpha)\sin(\beta)\sin(\gamma)p$  can be ignored because both pitch, roll, and  $p$  are small values, and the total contribution of the multiple is much less than 1 mm. Due to high nonlinearity, we do not derive detailed errors using time-varying heading/pitch/roll measurements. Instead, we apply loose constraints and derive possible maximum errors in the seafloor anchor position. For example,  $\cos(\alpha)$  or  $\sin(\alpha)$  in equations (A2–A4) should fall between  $-1$  and  $1$ , and they can counteract each other, but we allow their absolute values to be  $1$  at the same time; thus, the derived errors represent the maximum possible error. Formulas (A5–A7) show the possible amplitudes of anchor positioning errors. Among these, errors in heading measurements will not affect the vertical component of the anchor position estimates. An error in buoy length ( $L$ ) will result in a systematic error in vertical component of the anchor position but will be consistent for all vertical component estimates; hence, its influence on displacement estimates is trivial (Figure S8). Note that thermal expansion may induce additional error in buoy length but is small compared to the overall error budget and could be largely eliminated using a temperature-dependent model. At the test area, daily mean water temperature change between summer and winter is less than  $25^\circ\text{C}$  (Figure S9). The thermal expansion coefficient for steel is about  $1 \times 10^{-5}$  mm/K (Okaji et al., 2000); thus, thermal expansion-induced change in buoy length is on the order of a few mm.

Assuming that reasonable errors for initial anchor coordinates in reference frame  $G-X_b Y_b Z_b$  are 3, 3, and 30 cm (i.e.,  $p = \pm 3$  cm,  $q = \pm 3$  cm, and  $L = \pm 30$  cm), and using the repeatabilities provided by the digital compass manufacturer as errors for each heading/pitch/roll measurement (i.e.,  $\alpha = \pm 0.3^\circ$ ,  $\beta = \pm 0.2^\circ$ , and  $\gamma = \pm 0.2^\circ$  [HMR3000 data sheet from Honeywell International Inc. 2019]), the maximum possible errors caused by errors in  $p$ ,  $q$ ,  $L$ ,  $\alpha$ ,  $\beta$ , and  $\gamma$  are shown in formulas (A8–A10). For a single epoch, errors in horizontal displacement estimates are at the centimeter level and well below 1 cm for the vertical component. The SDs calculated for selected periods in Figure 11b are in approximate agreement with this theoretical analysis and hence are representative of the noise level in the daily displacement time series.

### 4.2. Response to Environmental Forcing

The GPS-buoy system rotates around the fixed anchor under the forcing of periodic tidal currents. Except for rapid motion during the first month after deployment due to settling, and the exceptionally rainy summer 2019, the anchor is relatively stable. Perturbations to anchor position occur mainly during extreme weather or periods of exceptionally high tidal current (Figures 10 and 12). These are analyzed below.

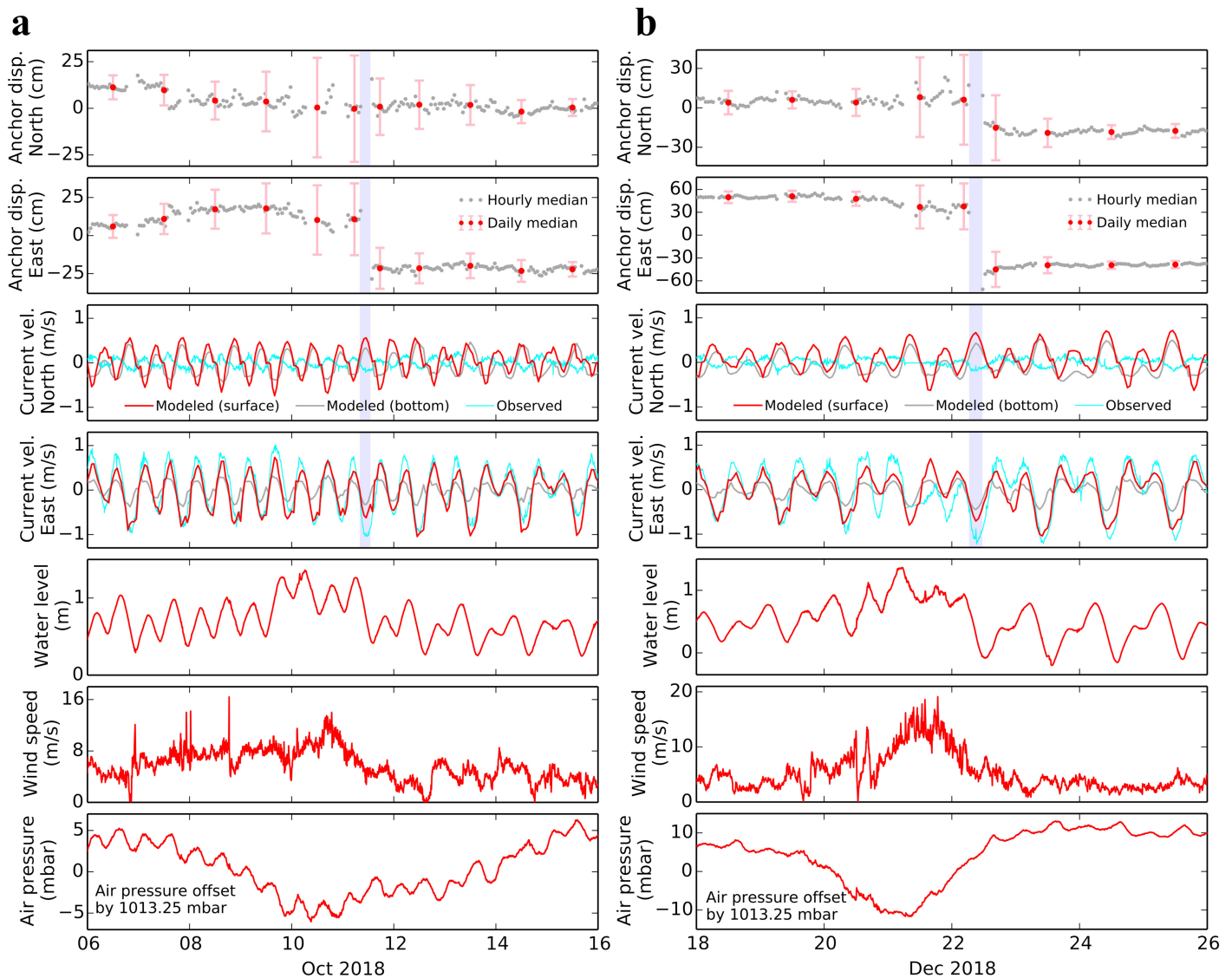


**Figure 12.** Anchor displacement and environmental variables during Hurricane Michael (a) and an unnamed storm in December 2018 (b). Water levels were observed at the site shown by the orange square in Figure 1b. Currents (Chen et al., 2018, 2019) are the Tampa Bay Coastal Ocean Model (TBCOM) hindcast at the GPS-buoy site. Observed currents were recorded by a current meter shown by the orange pentagon in Figure 1b. Wind speed and air pressure data were observed at the meteorological station shown by orange triangle in Figure 1b. Note that light blue shade marks the time of large displacement when current speed is at local maximum. The supporting information in Figure S10 shows anchor displacement and current along anchor long-term motion direction and local mean current direction, both showing that large anchor displacements occurred when current speeds are at local maximum.

For the GPS and digital compass, the most prominent signal is the quasi-diurnal motion associated with ocean tides (Figures 5–7). Large pitch/roll values occur during high-speed current periods (Figure 7b and Movies S1–S3). Figure 8 shows that most of the time, the GPS phase center is located northwest of the estimated anchor position, indicating that outgoing tidal currents are stronger than incoming tidal currents. This reflects the geometry of Tampa Bay (Figure 1b), where fresh water from the Hillsborough River watershed adds to outgoing currents associated with the ocean tide. The geometry of the deep Egmont shipping channel focuses a direct outward tidal flow (jet) directly toward the buoy and the northern end of Egmont Key as it exits Tampa Bay (Figure 1b).

The buoy anchor moved westward by several meters immediately after deployment. The largest displacement occurred during the first 2 days after deployment. After that, large displacements correlate with periods of extreme weather conditions (Figures 10, 12, and Figures S6 and S10). The United States Geological Survey coastal database shows that seafloor at the anchor location is primarily sand based (usSEABED database:



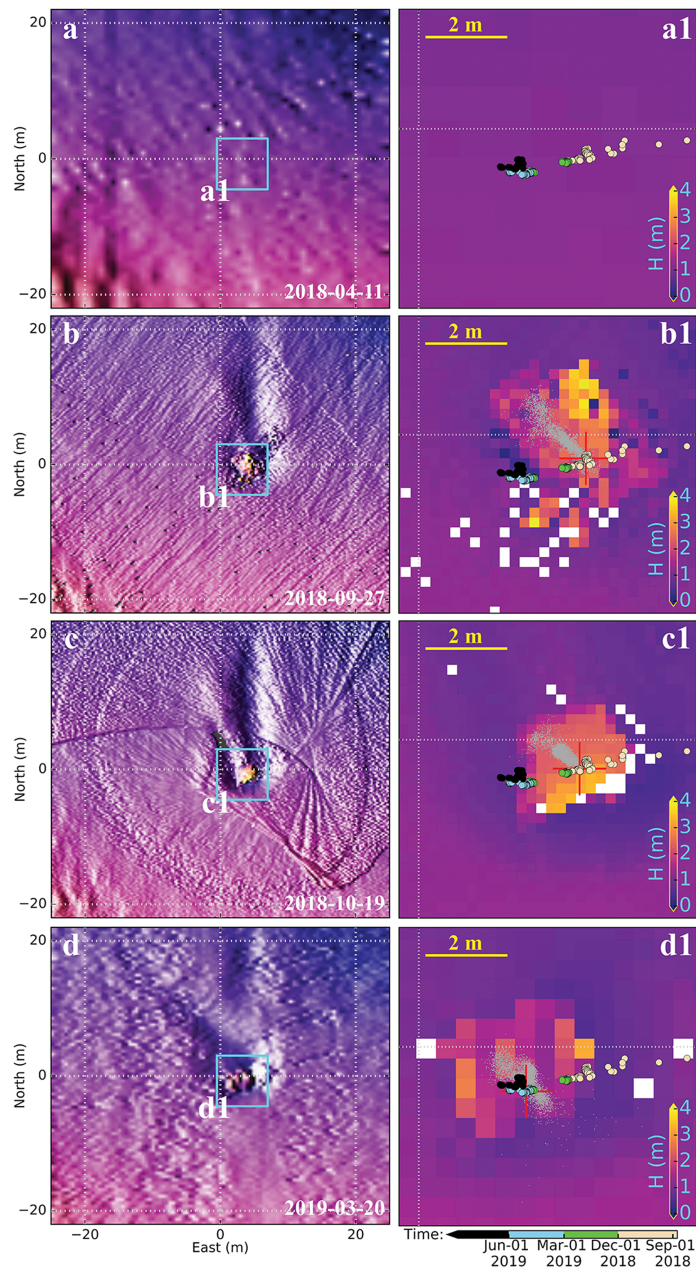


**Figure 13.** Bathymetry from multibeam sonar surveys showing bottom changes after buoy deployment. Hillshade maps (left column) are illuminated by a light source from west (azimuth angle is  $270^\circ$ , clockwise from north), with an elevation angle of  $30^\circ$ . White annotations on the lower right of (a, b, c, and d) show dates of surveys. Details of the outlined cyan box are shown on the right column. In a1, b1, c1, and d1, background color maps show relative heights with color bars changing from dark purple (deeper) to yellow (shallower); colored dots show daily median estimate of anchor positions with color bar change from wheat, green, to black (located at the bottom of (d1)). In b1, c1, and d1, gray dots show a 15-second interval GPS positions on corresponding days; centers of red “+” mark anchor position estimates for corresponding days. Note that bathymetry artifact in (c) is due to waves caused by ship turning, white pixels in b1, c1, and d1 are data gaps due to low density of valid sounding measurements. All maps are in the same local reference frame. The multibeam data set used to choose the buoy location from April 2018 was collected with a Reson SeaBat T50-R dual-head 200–400-kHz system, run at 400 kHz. The September 2018 data set was collected with a Reson SeaBat 7125, also run at 400 kHz. All following multibeam data sets were collected with the Reson SeaBat T50-R dual-head run at 400 kHz.

[https://coastalmap.marine.usgs.gov/js\\_map/national/usseabed/](https://coastalmap.marine.usgs.gov/js_map/national/usseabed/), also see Figure 2b). A bottom cavity (Figure 3) at the bottom of the ballast was designed to minimize translation movements on such bottom types, which should give a friction coefficient ( $f$ ) of  $\sim 0.7$  (IALA guideline 1066, 2010; geotechdata.info, last

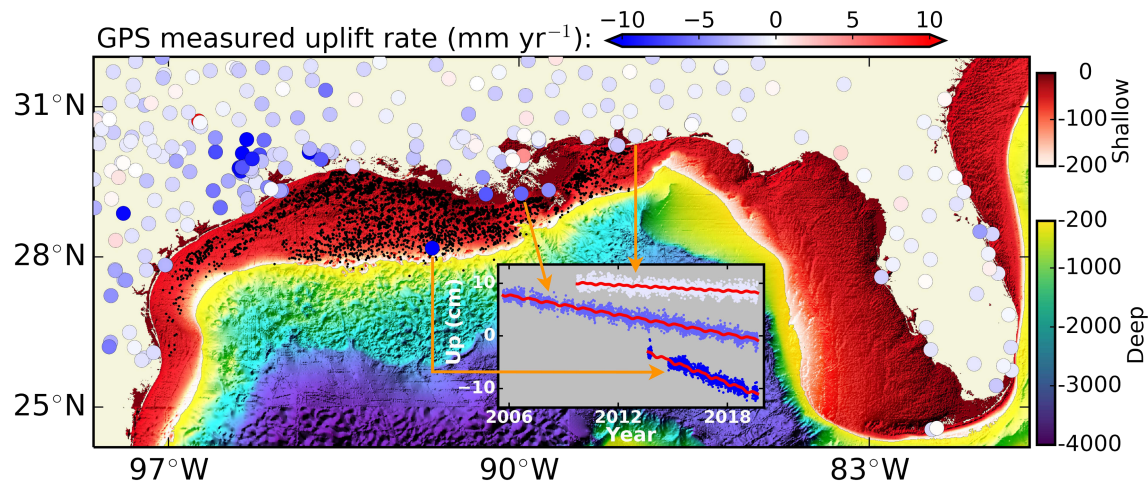


**Figure 14.** Bathymetry of the Gulf of Mexico. Colored dots show vertical displacement rate at continuous GPS stations (stations with >5-year observations are used; Blewitt et al., 2018). Black dots show locations of offshore oil platforms by January 2019 (data downloaded from Bureau of Ocean Energy Management at <https://www.data.boem.gov/Main/Mapping.aspx>). Insert shows vertical displacements of three continuous GPS stations (offset for clarity), scatter are GPS daily time series (step changes due to large earthquakes, antenna replacements, and reference frame changes are corrected; Blewitt et al., 2018), and red curves are best-fitting curves considering long-term trend and annual and semiannual variations.

access on 19 June 2019). Using a software mechanical model (Working Model™), and assuming a wind speed of 20–25 m/s plus an ocean flow speed of 1.1–1.8 m/s during extreme weather conditions (e.g., the unnamed storm around December 20, 2018), motion of the ballast is unlikely if the ballast sits on a gentle slope (ballast tilt angle less than several degrees), due to a residual frictional force of  $>1.0 \times 10^4$  N (Figure S11). Models with much lower friction ( $f = 0.3$ ) suggest that ballast motion is possible under conditions of high tidal current forcing (Figure S11b). Additional modeling results suggest that the optimum site condition for the present design is a dense sand bed with slope smaller than  $5^\circ$  and current speed less than 2 m/s.

At the test site, current-induced scour changes conditions at the buoy anchor and is the most likely cause of the displacements. The left column of Figure 13 shows hillshade maps of the GPS-buoy site derived from multibeam sonar surveys. Large troughs formed near the anchor, probably contributing to anchor instabilities. The bathymetry data derived from multibeam surveys have grid sizes of 0.25–0.5 m, depending on the density of sounding measurements. Geolocations of these bathymetry maps (with Marinestar) have an accuracy of about 0.1 m (<https://www.fugro.com/our-services/marine-asset-integrity/satellite-positioning/marinestar>). Comparison of multibeam sonar soundings of the anchor in the 27 September 2018 surface to the 20 March 2019 surface shows a southwestern displacement of 1–2 m, consistent with the anchor position estimates using the GPS-buoy system (figure 13).

Diver observations on 1 October 2019 support this view. They show the anchor sitting in a 1-m-deep scour hole, with a gap at one corner between the base of the anchor and the sediment water interface. This suggests that the anchor periodically shifts after periods of high current speeds and scour activity, settling into a new position as scour activity changes the local slope beneath the anchor.

Most applications of the buoy would not involve locations in a tidal channel, so these kinds of perturbations would not likely occur. For applications where high tidal current speeds are expected, modification of the ballast design may be required.

#### 4.3. Complementarity to Existing Seafloor Geodesy Methods

Several methods have been developed to measure seafloor motion, including the following:

1. Bottom pressure (e.g., Chadwick et al., 2006; Chierici et al., 2016)
2. GPS acoustic (e.g., Chadwell & Spiess, 2008; Sato et al., 2011; Spiess, 1985; Spiess et al., 1998; Yokota et al., 2016)
3. Direct-path acoustic ranging (e.g., Chadwick & Stapp, 2002; Osada et al., 2012; McGuire & Collins, 2013)

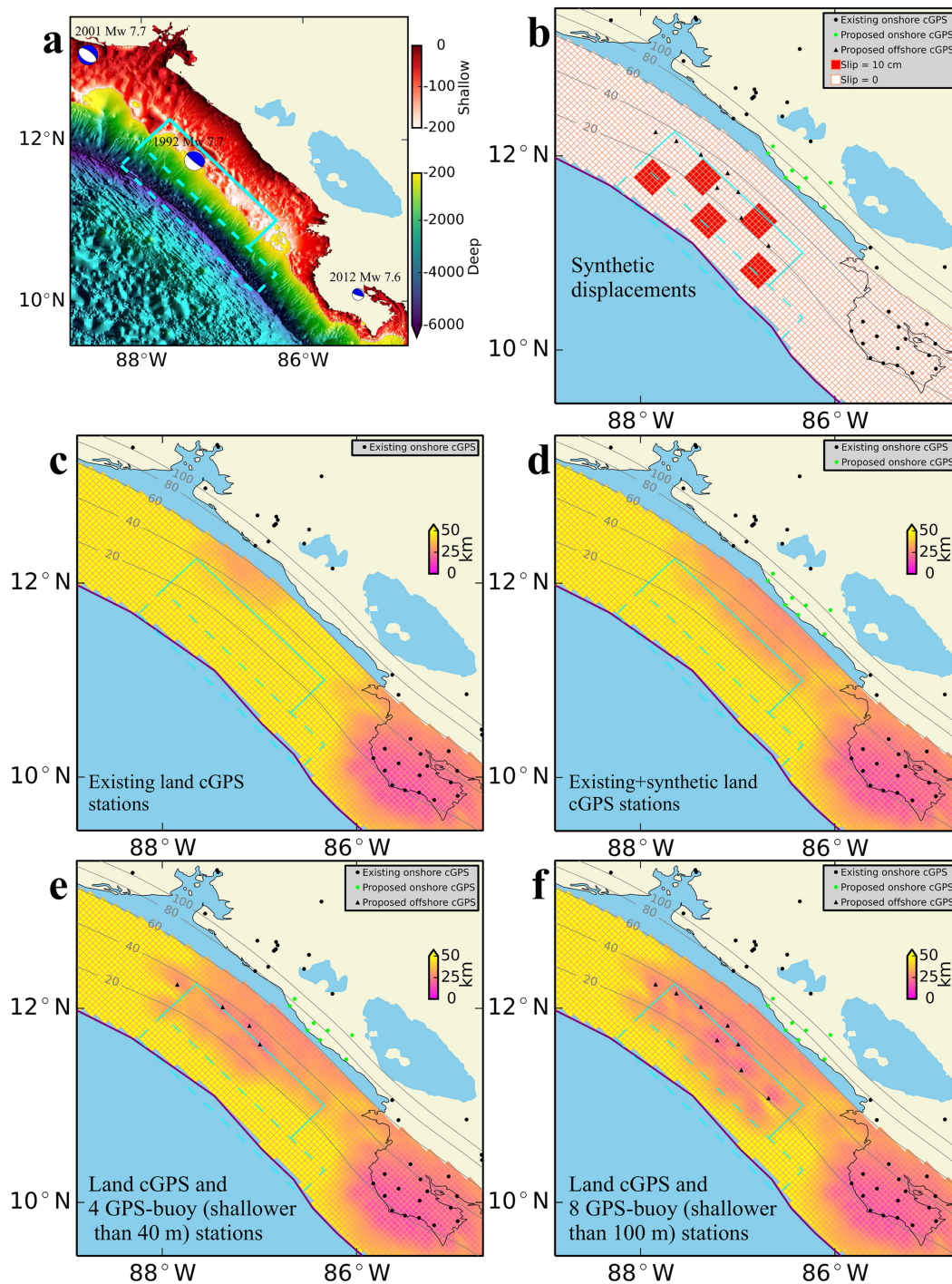


**Figure 15.** Potential application area in Central America. (a) Bathymetry of the fore-arc region in Central America. Beach balls show  $M_w > 7.5$  earthquakes between 1 January 1980 and 1 March 2019. Dashed-line box outlines the 1992 Nicaragua earthquake tsunami fault model by Satake (1994). Solid line box outlines the seismological fault model by Ide et al. (1993), adopted from Figure 1 in Satake (1994). (b–f) Resolution test of slip inversion with/without seafloor geodetic measurements. Horizontal size of each small patch is  $5 \text{ km} \times 5 \text{ km}$ . Black dots are existing continuous GPS (cGPS) on land, green dots are proposed cGPS on land (P. La Femina, personal communication), and black triangles are synthetic GPS-buoy sites. Purple lines mark location of the trench. Gray lines are slab depth contour (in km, Hayes et al., 2018). Land GPS and offshore GPS sites are weighted with different uncertainties: Land GPS north (0.2 cm), east (0.2 cm), and vertical (0.4 cm) directions and offshore GPS north (2.0 cm), east (2.0 cm), and vertical (0.5 cm) directions. (c) shows resolution length scale with existing land cGPS stations. (d) shows resolution length scale with existing land cGPS stations plus 8 synthetic land cGPS stations. (e) shows resolution length scale with land cGPS plus four synthetic offshore GPS-buoy stations (shallower than 40 m). (f) shows resolution length scale with land cGPS plus eight synthetic offshore GPS-buoy stations (shallower than 100 m). For comparison, resolution remains unchanged in Nicoya Peninsula, Costa Rica (lower right), consistent with the model resolution of Kyriakopoulos and Newman (2016).

4. Multibeam sonar surveying (e.g., DeSanto et al., 2016; Fujiwara et al., 2017)
5. Strainmeter and tiltmeter systems (e.g., Anderson et al., 1997; Zumberge et al., 2018)

While all of these techniques are applicable in certain situations, they would have limitations in shallow, turbulent coastal water due to oceanographic noise. Our GPS-buoy system overcomes these difficulties and thus complements existing methods.

#### 4.4. Potential Application in Shallow Water Seafloor Geodesy

Our GPS-buoy system has a number of applications in the shallow continental shelf environment and active margins. In regions of offshore petroleum extraction, a sparse network could help define the deformation pattern around oil and natural gas reservoirs as these products are extracted (Figure 14). Depleted offshore reservoirs have been proposed as possible sites for carbon capture and storage. Monitoring the surface deformation that occurs in these reservoirs as CO<sub>2</sub> is added can help to assess reservoir integrity (Karegar, Dixon, Malservisi, Yang, et al., 2015; Yang et al., 2015).

The Mississippi Delta (Figure 14) has long been recognized as an area experiencing subsidence and land loss, due to a combination of natural and human-induced causes (e.g., Morton et al., 2006; Yuill et al., 2009). Compaction of younger Holocene sediments may be a significant cause (e.g., Meckel, 2008; Törnqvist et al., 2008). If dominant, then subsidence rate should correlate with the thickness of the underlying Holocene section (e.g., Figure 2a in Karegar, Dixon, & Malservisi, 2015). Some offshore areas in the delta can have considerably thicker Holocene sections compared to on-land areas; hence measuring offshore subsidence could help to better define the processes contributing to subsidence, assuming that initial subsidence of the anchor during the settling period was accounted for.

Volcano monitoring with the system is well described in De Martino et al. (2014) and Iannaccone et al. (2018). In some volcano-tectonic regions, shallow water environments preclude precise measurement of strain or displacement fields. A good example is Lago Nicaragua in southern Nicaragua. The lake occupies more than 8,000 km<sup>2</sup>, and limits measurement of surface deformation there except in a few marginal areas. The majority of the lake is shallower than 40-m depth and hence is amenable to geodetic measurements with the current system.

In subduction zones, many of the largest earthquakes occur offshore. Offshore strain accumulation and release processes are critical for understanding megathrust earthquakes and tsunamis but are usually poorly monitored. Parts of the Central America subduction system have a large shallow water section. In Nicaragua, for example, nearly 50% of the area between the coastline and the trench is shallower than 150 m (Figure 15a). In the Nicoya Peninsula of Costa Rica, Dixon et al. (2014) found that shallow slow slip events during the interseismic period release a significant amount of accumulated strain, perhaps reducing earthquake magnitude and tsunami potential. Similar results have been observed offshore Ecuador (Rolandone et al., 2018). Our GPS-buoy system is a promising geodetic tool to monitor seafloor motion in these shallow fore-arc regions.

Figure 15 shows an example of how such a system could improve slip resolution of offshore events. Figure 15a shows the bathymetry of the fore-arc region in Central America. 10-cm dip slips were simulated on the plate interface (red patches). Figures 15c–15f show model resolution length scales with different data sets, based on Funning et al. (2005). Smoothing parameters used in Figures 15c–15f are the same, based on existing onshore continuous GPS data. An elastic half-space model (Okada, 1992) is used to calculate Green functions, and the Tikhonov regularization method is used to maximize smoothing while minimizing residuals, similar to Malservisi et al. (2015). Even with numerous continuous GPS stations on land (Figures 15c and 15d), slip distribution near the trench is not well resolved. Adding a relatively small number of GPS-buoy stations at selected shallow locations significantly improves the resolution of estimated slip distribution offshore (Figures 15e and 15f).

## 5. Conclusions

We have developed a GPS-buoy system suitable for measuring horizontal and vertical components of shallow water seafloor motion. The system consists of a GPS station, a digital compass, a spar buoy anchored to seafloor by a heavy ballast, and a float integrated into the spar. GPS data are processed in the kinematic mode, and a three-dimensional transformation is used to estimate anchor position based on GPS position

and buoy heading/pitch/roll measurements. During a test period in Tampa Bay, the system successfully recorded transient events associated with Hurricane Michael and other heavy precipitation events, when current speeds are high. For a single measurement, uncertainty induced by errors in buoy geometry and digital compass measurements is at the centimeter level. Using a median filter, the daily position time series of the anchor have a repeatability of 1–2 cm or better for the three position components. This system can be applied to a variety of study areas, including offshore regions of subduction zones for measuring strain accumulation and release processes. A combination of on-land GPS, GPS buoys in shallow water, and GPS-acoustic systems or pressure gauges in deep water would provide complete geodetic coverage for subduction zone earthquake and tsunami and volcano hazard studies.

### Appendix A. Errors on Anchor Positioning Induced by Buoy Structure and Digital Compass Measurement Errors

Considering errors in GPS-buoy geometry used for anchor position estimates, and substituting the three rotation matrix, equation (2) becomes

$$\begin{bmatrix} N_{ag} \\ E_{ag} \\ U_{ag} \end{bmatrix} = \begin{bmatrix} \cos(\alpha)\cos(\beta) & \cos(\alpha)\sin(\beta)\sin(\gamma) - \sin(\alpha)\cos(\gamma) & \cos(\alpha)\sin(\beta)\cos(\gamma) + \sin(\alpha)\sin(\gamma) \\ \sin(\alpha)\cos(\beta) & \sin(\alpha)\sin(\beta)\sin(\gamma) + \cos(\alpha)\cos(\gamma) & \sin(\alpha)\sin(\beta)\cos(\gamma) - \cos(\alpha)\sin(\gamma) \\ -\sin(\beta) & \cos(\beta)\sin(\gamma) & \cos(\beta)\cos(\gamma) \end{bmatrix} \begin{bmatrix} p \\ q \\ L \end{bmatrix}. \quad (A1)$$

Assuming  $p$ ,  $q$ ,  $L$ ,  $\alpha$ ,  $\beta$ , and  $\gamma$  are independent parameters, partial derivatives of equation (A1) are shown in equations (A2–A4).

$$\left\{ \begin{array}{l} \frac{\partial N_{ag}}{\partial p} = \cos(\alpha)\cos(\beta) \\ \frac{\partial N_{ag}}{\partial q} = \cos(\alpha)\sin(\beta)\sin(\gamma) - \sin(\alpha)\cos(\gamma) \\ \frac{\partial N_{ag}}{\partial L} = \cos(\alpha)\sin(\beta)\cos(\gamma) + \sin(\alpha)\sin(\gamma) \\ \frac{\partial N_{ag}}{\partial \alpha} = -p\sin(\alpha)\cos(\beta) - q\sin(\alpha)\sin(\beta)\sin(\gamma) - q\cos(\alpha)\cos(\gamma) - L\sin(\alpha)\sin(\beta)\cos(\gamma) + L\cos(\alpha)\sin(\gamma) \\ \frac{\partial N_{ag}}{\partial \beta} = -p\cos(\alpha)\sin(\beta) + q\cos(\alpha)\cos(\beta)\sin(\gamma) + L\cos(\alpha)\cos(\beta)\cos(\gamma) \\ \frac{\partial N_{ag}}{\partial \gamma} = q\cos(\alpha)\sin(\beta)\sin(\gamma) + q\sin(\alpha)\sin(\gamma) - L\cos(\alpha)\sin(\beta)\sin(\gamma) + L\sin(\alpha)\cos(\gamma) \end{array} \right. \quad (A2)$$

$$\left\{ \begin{array}{l} \frac{\partial E_{ag}}{\partial p} = \sin(\alpha)\cos(\beta) \\ \frac{\partial E_{ag}}{\partial q} = \sin(\alpha)\sin(\beta)\sin(\gamma) + \cos(\alpha)\cos(\gamma) \\ \frac{\partial E_{ag}}{\partial L} = \sin(\alpha)\sin(\beta)\cos(\gamma) - \cos(\alpha)\sin(\gamma) \\ \frac{\partial E_{ag}}{\partial \alpha} = p\cos(\alpha)\cos(\beta) + q\cos(\alpha)\sin(\beta)\sin(\gamma) - q\sin(\alpha)\cos(\gamma) + L\cos(\alpha)\sin(\beta)\cos(\gamma) + L\sin(\alpha)\sin(\gamma) \\ \frac{\partial E_{ag}}{\partial \beta} = -p\sin(\alpha)\sin(\beta) + q\sin(\alpha)\cos(\beta)\sin(\gamma) + L\sin(\alpha)\cos(\beta)\cos(\gamma) \\ \frac{\partial E_{ag}}{\partial \gamma} = q\sin(\alpha)\sin(\beta)\cos(\gamma) - q\cos(\alpha)\sin(\gamma) - L\sin(\alpha)\sin(\beta)\sin(\gamma) - L\cos(\alpha)\cos(\gamma) \end{array} \right. \quad (A3)$$

$$\left\{ \begin{array}{l} \frac{\partial U_{ag}}{\partial p} = -\sin(\beta) \\ \frac{\partial U_{ag}}{\partial q} = \cos(\beta)\sin(\gamma) \\ \frac{\partial U_{ag}}{\partial L} = \cos(\beta)\sin(\gamma) \\ \frac{\partial U_{ag}}{\partial \alpha} = 0 \\ \frac{\partial U_{ag}}{\partial \beta} = -p\cos(\beta) - q\sin(\beta)\sin(\gamma) - L\sin(\beta)\cos(\gamma) \\ \frac{\partial U_{ag}}{\partial \gamma} = q\cos(\alpha)\cos(\gamma) - L\cos(\beta)\sin(\gamma) \end{array} \right. \quad (A4)$$

After ignoring items that are insignificant in total error budgets, formulas (A5–A7) show the maximum range of possible errors induced by corresponding parameters. In these formulas,  $N_{ag|p}$  denotes error in northern component of the anchor position caused by error in  $p$  and so forth. Note that all items are simplified to be positive values in formulas (A5–A7) and pitch and roll measurements between  $-2^\circ$  and  $2^\circ$  are used. The derived values are maximum possible errors.

$$\left\{ \begin{array}{l} \Delta N_{ag}|_{\Delta p} \leq \Delta p \\ \Delta N_{ag}|_{\Delta q} \leq [\sin(\alpha)]\Delta q \leq \Delta q \\ \Delta N_{ag}|_{\Delta L} \leq [\sin(\beta) + \sin(\gamma)]\Delta L < [\sin(2^\circ) + \sin(2^\circ)]\Delta L = 0.07\Delta L \\ \Delta N_{ag}|_{\Delta \alpha} \leq [p + q + L\sin(\beta) + L\sin(\gamma)]\Delta \alpha < [p + q + L\sin(2^\circ) + L\sin(2^\circ)]\Delta \alpha = [p + q + 0.07L]\Delta \alpha \\ \Delta N_{ag}|_{\Delta \beta} \leq [p\sin(\beta) + q\sin(\gamma) + L]\Delta \beta < [p\sin(2^\circ) + q\sin(2^\circ) + L]\Delta \beta = [0.035p + 0.035q + L]\Delta \beta \\ \Delta N_{ag}|_{\Delta \gamma} \leq [q\sin(\beta) + q\sin(\gamma) + L]\Delta \gamma < [q\sin(2^\circ) + q\sin(2^\circ) + L]\Delta \gamma = [0.07q + L]\Delta \gamma \end{array} \right. \quad (A5)$$

$$\left\{ \begin{array}{l} \Delta E_{ag}|_{\Delta p} \leq [\sin(\alpha)]\Delta p \leq \Delta p \\ \Delta E_{ag}|_{\Delta q} \leq \Delta q \\ \Delta E_{ag}|_{\Delta L} \leq [\sin(\beta) + \sin(\gamma)]\Delta L < [\sin(2^\circ) + \sin(2^\circ)]\Delta L = 0.07\Delta L \\ \Delta E_{ag}|_{\Delta \alpha} \leq [p + q + L\sin(\beta) + L\sin(\gamma)]\Delta \alpha < [p + q + L\sin(2^\circ) + L\sin(2^\circ)]\Delta \alpha = [p + q + 0.07L]\Delta \alpha \\ \Delta E_{ag}|_{\Delta \beta} \leq [p\sin(\beta) + q\sin(\gamma) + L]\Delta \beta < [p\sin(2^\circ) + q\sin(2^\circ) + L]\Delta \beta = [0.035p + 0.035q + L]\Delta \beta \\ \Delta E_{ag}|_{\Delta \gamma} \leq [q\sin(\beta) + q\sin(\gamma) + L]\Delta \gamma < [q\sin(2^\circ) + q\sin(2^\circ) + L]\Delta \gamma = [0.07q + L]\Delta \gamma \end{array} \right. \quad (A6)$$

$$\left\{ \begin{array}{l} \Delta U_{ag}|_{\Delta p} < [\sin(2^\circ)]\Delta p = 0.035\Delta p \\ \Delta U_{ag}|_{\Delta q} \leq [\sin(\gamma)]\Delta q < [\sin(2^\circ)]\Delta q = 0.035\Delta q \\ 0.9988\Delta L = [\cos(2^\circ)\cos(2^\circ)]\Delta L < \Delta U_{ag}|_{\Delta \alpha} \leq \Delta L \\ \Delta U_{ag}|_{\Delta \alpha} = 0 \\ \Delta U_{ag}|_{\Delta \beta} \leq [p + L\sin(\beta)]\Delta \beta < [p + L\sin(2^\circ)]\Delta \beta = [p + 0.035L]\Delta \beta \\ \Delta U_{ag}|_{\Delta \gamma} \leq [q + L\sin(\gamma)]\Delta \gamma < [q + L\sin(2^\circ)]\Delta \gamma = [q + 0.035L]\Delta \gamma \end{array} \right. \quad (A7)$$

Given input errors as  $p = \pm 3$  cm,  $q = \pm 3$  cm,  $L = \pm 30$  cm,  $\alpha = \pm 0.3^\circ$ ,  $\beta = \pm 0.2^\circ$ , and  $\gamma = \pm 0.2^\circ$ . Formulas (A8–A10) show the range of propagated errors in anchor position estimates.

**Acknowledgments**

This research was mainly supported by NSF-OTIC grant 1538179 to THD. Additional funding includes NFWF grant 45892 and NOAA grant NA16OAR4170181. We acknowledge Prospero DeMartino and Gianpaolo Donnarumma at INGV/Italy for helpful discussions and Nicolas Bayou from UNAVCO for technical support. The USF-CMS Center for Ocean Technology provided critical electrical and systems engineering for the project. Hydra Solutions of Italy designed the buoy and assisted with deployment plans. We thank the Florida Institute of Oceanography for logistical support during the deployment of the SUBGEO system. We acknowledge Robert Weisberg and the USF Ocean Circulation Lab for providing logistical support, real-time data posting, and model output from their high-resolution Tampa Bay Coastal Ocean Model (TBCOM). Ben Meister, Sebastian DiGeronimo, Mitchell Hastings, Steve Murawski, Steve Butcher, Stan Locker, the Captains, and crews of the RV Weatherbird, Hogarth and Price are thanked for their help with the field work. Buoy deployment was performed by Orion Marine Group (<http://www.orionmarinegroup.com/>). GPS and heading/pitch/roll measurements are archived at UNAVCO (<https://doi.org/10.7283/TM3V-P845>) and are publicly available. Reference GPS station MCD5 belongs to the Continuously Operating Reference Station (CORS) operated by NOAA/NGS (<https://www.ngs.noaa.gov/CORS/>). Bathymetry data used in Figures 1b, 14, and 15a were downloaded from the General Bathymetric Chart of the Oceans (GEBCO, <https://www.gebco.net/>). Water level and current data were downloaded from NOAA Tides and Currents (<https://tidesandcurrents.noaa.gov/ports/index.html?port=tb>). Precipitation data were downloaded from NOAA's National Centers for Environment Information website (<https://www.ncei.noaa.gov/>). World Magnetic Model was downloaded from NOAA website (<https://www.ngdc.noaa.gov/geomag/WMM/soft.shtml#downloads>). OpenCV-Python (<https://opencv-python-tutroals.readthedocs.io/en/latest/index.html>) was used to do the inverse perspective transformation. We thank Tom Herring and Robert King for maintenance of the GAMIT/GLOBK/TRACK software and the Canadian Spatial Reference System (CSRS, <https://webapp.geod.nrcan.gc.ca/geod/tools-outils/ppp.php?locale=en>) for providing their online GPS processing tool.

$$\left\{ \begin{array}{l} \Delta N_{ag} |_{\Delta p} \leq 0.030 \text{ m} \\ \Delta N_{ag} |_{\Delta q} \leq 0.030 \text{ m} \\ \Delta N_{ag} |_{\Delta L} < 0.021 \text{ m} \\ \Delta N_{ag} |_{\Delta \alpha} < 0.010 \text{ m} \\ \Delta N_{ag} |_{\Delta \beta} < 0.096 \text{ m} \\ \Delta N_{ag} |_{\Delta \gamma} < 0.096 \text{ m} \end{array} \right. \quad (A8)$$

$$\left\{ \begin{array}{l} \Delta E_{ag} |_{\Delta p} \leq 0.030 \text{ m} \\ \Delta E_{ag} |_{\Delta q} \leq 0.030 \text{ m} \\ \Delta E_{ag} |_{\Delta L} < 0.021 \text{ m} \\ \Delta E_{ag} |_{\Delta \alpha} < 0.010 \text{ m} \\ \Delta E_{ag} |_{\Delta \beta} < 0.096 \text{ m} \\ \Delta E_{ag} |_{\Delta \gamma} < 0.096 \text{ m} \end{array} \right. \quad (A9)$$

$$\left\{ \begin{array}{l} \Delta U_{ag} |_{\Delta p} < 0.001 \text{ m} \\ \Delta U_{ag} |_{\Delta q} < 0.001 \text{ m} \\ 0.2996 \text{ m} < \Delta U_{ag} |_{\Delta L} < 0.300 \text{ m} \\ \Delta U_{ag} |_{\Delta \alpha} = 0 \text{ m} \\ \Delta U_{ag} |_{\Delta \beta} < 0.003 \text{ m} \\ \Delta U_{ag} |_{\Delta \gamma} < 0.003 \text{ m} \end{array} \right. \quad (A10)$$

**References**

Anderson, G., Constable, S., Staudigel, H., & Wyatt, F. K. (1997). A seafloor long-baseline tiltmeter. *Journal of Geophysical Research*, 102(B9), 20,269–20,285.

Berman, G. A., Naar, D. F., Hine, A. C., Brooks, G. R., Tebbens, S. F., Donahue, B. T., & Wilson, R. (2005). Geologic structure and hydrodynamics of Egmont Channel: An anomalous inlet at the mouth of Tampa Bay, Florida. *Journal of Coastal Research*, 21(2), 331–357.

Blewitt, G., Hammond, W. C., & Kreemer, C. (2018). Harnessing the GPS data explosion for interdisciplinary science. *Eos*, 99. <https://doi.org/10.1029/2018EO104623>

Bock, Y., & Melgar, D. (2016). Physical applications of GPS geodesy: A review. *Reports on Progress in Physics*, 79, 106801.

Brooks, G. R., & Doyle, L. J. (1998). Recent sedimentary development of Tampa Bay, Florida: A microtidal estuary incised into tertiary platform carbonates. *Estuaries*, 21(3), 391–406.

Bürgmann, R., & Chadwell, D. (2014). Sea floor geodesy. *Annual Review of Earth and Planetary Sciences*, 42, 509–534. <https://doi.org/10.1146/annurev-earth-060313-054953>

Chadwell, C. D., & Spiess, F. N. (2008). Plate motion at the ridge-transform boundary of the south cleft segment of the Juan de Fuca Ridge from GPS-acoustic data. *Journal of Geophysical Research*, 113, B04415. <https://doi.org/10.1029/2007JB004936>

Chadwick, W. W., Nooner, S. L., Zumberge, M. A., Embley, R. W., & Fox, C. G. (2006). Vertical deformation monitoring at axial seamount since its 1998 eruption using deep-sea pressure sensors. *Journal of Volcanology and Geothermal Research*, 150(1), 313–327. <https://doi.org/10.1016/j.jvolgeores.2005.07.006>

Chadwick, W. W. Jr., & Stapp, M. (2002). A deep-sea observatory experiment using acoustic extensometers: Precise horizontal distance measurements across a mid-ocean ridge. *IEEE Journal of Oceanic Engineering*, 27(2), 193–201.

Chen, G. (1998). GPS kinematic positioning for the airborne laser altimetry at Long Valley, California. *Doctoral Dissertation, Mass. Inst. of Technol.*

Chen, J., Weisberg, R. H., Liu, Y., & Zheng, L. (2018). The Tampa Bay coastal ocean model performance for Hurricane Irma. *Marine Technology Society Journal*, 52(3), 33–42. <https://doi.org/10.4031/MTSJ.52.3.6>

Chen, J., Weisberg, R. H., Liu, Y., Zheng, L., & Zhu, J. (2019). On the momentum balance of Tampa Bay. *Journal of Geophysical Research: Oceans*, 124, 4492–4510. <https://doi.org/10.1029/2018JC014890>

Chierici, F., Iannaccone, G., Pignagnoli, L., Guardato, S., Locritani, M., Embriaco, D., et al. (2016). A new method to assess long-term sea-bottom vertical displacement in shallow water using a bottom pressure sensor: Application to Campi Flegrei, southern Italy. *Journal of Geophysical Research: Solid Earth*, 121, 7775–7789. <https://doi.org/10.1002/2016JB013459>

Davis, J. L., De Juan, J., Nettles, M., Elosegui, P., & Andersen, M. L. (2014). Evidence for non-tidal diurnal velocity variations of Helheim Glacier, east Greenland. *Journal of Glaciology*, 60(224), 1169–1180.

De Martino, P., Guardato, S., Tammara, U., Vassallo, M., & Iannaccone, G. (2014). A first GPS measurement of vertical sea floor displacement in the Campi Flegrei caldera (Italy). *Journal of Volcanology and Geothermal Research*, 276, 145–151. <https://doi.org/10.1016/j.jvolgeores.2014.03.003>

DeSanto, J. B., Sandwell, D. T., & Chadwell, C. D. (2016). Sea floor geodesy from repeated sidescan sonar surveys. *Journal of Geophysical Research: Solid Earth*, 121, 4800–4813. <https://doi.org/10.1002/2016JB013025>

- Dixon, T. H. (1991). An introduction to the global positioning system and some geological applications. *Reviews of Geophysics*, 29(2), 249–276. <https://doi.org/10.1029/91RG00152>
- Dixon, T. H., Jiang, Y., Malservisi, R., McCaffrey, R., Voss, N., Protti, M., & Gonzalez, V. (2014). Earthquake and tsunami forecasts: Relation of slow slip events to subsequent earthquake rupture. *National Academy of Sciences of the United States of America*, 111(48), 17,039–17,044.
- Dixon, T. H., Xie, S., Law, J., Russell, R., Malservisi, R., Lembke, C. (2019). SUBGEO, UNAVCO, Inc., GPS/GNSS observations dataset, <https://doi.org/10.7283/TM3V-P845>.
- Doyle, L. J., & Sparks, T. N. (1980). Sediments of the Mississippi, Alabama, and Florida (MAFLA) continental shelf. *Journal of Sedimentary Research*, 50(3), 905–915.
- Evans, M. W., Hine, A. C., Belknap, D. F., & Davis, R. A. Jr. (1985). Bedrock controls on barrier island development: West-central Florida coast. *Marine Geology*, 63(1-4), 263–283.
- Fujiwara, T., Santos Ferreira, C., Bachmann, A. K., Strasser, M., Wefer, G., Sun, T., et al. (2017). Seafloor displacement after the 2011 Tohoku-Oki earthquake in the northern Japan trench examined by repeated bathymetric surveys. *Geophysical Research Letters*, 44, 11,833–11,839. <https://doi.org/10.1002/2017GL075839>
- Funning, G. J., Parsons, B., Wright, T. J., Jackson, J. A., & Fielding, E. J. (2005). Surface displacements and source parameters of the 2003 Bam (Iran) earthquake from Envisat advanced synthetic aperture radar imagery. *Journal of Geophysical Research*, 110, B09406. <https://doi.org/10.1029/2004JB003338>
- Ginsburg, R. N., & James, N. P. (1974). Holocene carbonate sediments of continental shelves. In *The geology of continental margins*, (pp. 137–155). Berlin, Heidelberg: Springer.
- Gray, J. W. (2018). The stability of sand waves in a tidally influenced shipping channel, Tampa Bay, Florida. *Master's Thesis, University of South Florida, Tampa, FL*. <http://scholarcommons.usf.edu/etd/7157>
- Hayes, G. P., Moore, G. L., Portner, D. E., Hearne, M., Flamme, H., Furtney, M., & Smoczyk, G. M. (2018). Slab2, a comprehensive subduction zone geometry model. *Science*, 362(6410), 58–61. <https://doi.org/10.1126/science.aat4723>
- Herring, T. A., King, R. W., Floyd, A. A., & McClusky, S. C. (2018). GAMIT Reference Manual, GPS Analysis at MIT, Release 10.7. *Mass. Inst. of Technol., Cambridge*.
- Herring, T. A., Melbourne, T. I., Murray, M. H., Floyd, M. A., Szeliga, W. M., King, R. W., et al. (2016). Plate boundary observatory and related networks: GPS data analysis methods and geodetic products. *Reviews of Geophysics*, 54, 759–808. <https://doi.org/10.1002/2016RG000529>
- Hine, A. C. (1997). *Structural and paleoceanographic evolution of the margins of the Florida platform*. (pp. 169–194). Gainesville: The Geology of Florida. University Press of Florida.
- Hine, A. C. (2013). *Geologic history of Florida: Major events that formed the sunshine state*. Tampa, FL: University Press of Florida.
- Hine, A. C., Halley, R. B., Locker, S. D., Jarrett, B. D., Jaap, W. C., Mallinson, D. J., et al. (2008). Coral reefs, present and past, on the west Florida shelf and platform margin. In *Coral Reefs of the USA*, (pp. 127–173). Dordrecht: Springer.
- HMR3000 data sheet from Honeywell International Inc (2019). Digital compass solution HMR3000. [https://aerospace.honeywell.com/en/~media/aerospace/files/datasheet/digitalcompasssolutionhmr3000\\_ds.pdf](https://aerospace.honeywell.com/en/~/media/aerospace/files/datasheet/digitalcompasssolutionhmr3000_ds.pdf), last access on 23 September 2019.
- IALA Guideline 1066 (2010). Design of floating aid to navigation moorings. Edition 1.1.
- Iannaccone, G., Guardato, S., Donnarumma, G. P., De Martino, P., Dolce, M., Macedonio, G., et al. (2018). Measurement of seafloor deformation in the marine sector of the Campi Flegrei Caldera (Italy). *Journal of Geophysical Research: Solid Earth*, 123, 66–83. <https://doi.org/10.1002/2017JB014852>
- Ide, S., Imamura, F., Yoshida, Y., & Abe, K. (1993). Source characteristics of the Nicaraguan tsunami earthquake of 2 September 1992. *Geophysical Research Letters*, 20(9), 863–866.
- Iglewicz, B., & Hoaglin, D. C. (1993). *How to detect and handle outliers*. Milwaukee, WI: Asq Press.
- Karegar, M. A., Dixon, T. H., & Malservisi, R. (2015). A three-dimensional surface velocity field for the Mississippi Delta: Implications for coastal restoration and flood potential. *Geology*, 43(6), 519–522.
- Karegar, M. A., Dixon, T. H., Malservisi, R., Yang, Q., Hossaini, S. A., & Hovorka, S. D. (2015). GPS-based monitoring of surface deformation associated with CO<sub>2</sub> injection at an enhanced oil recovery site. *International Journal of Greenhouse Gas Control*, 41, 116–126.
- Kyriakopoulos, C., & Newman, A. V. (2016). Structural asperity focusing locking and earthquake slip along the Nicoya megathrust, Costa Rica. *Journal of Geophysical Research: Solid Earth*, 121, 5461–5476. <https://doi.org/10.1002/2016JB012886>
- Larson, K. M., Lowry, A. R., Kostoglodov, V., Hutton, W., Sánchez, O., Hudnut, K., & Suárez, G. (2004). Crustal deformation measurements in Guerrero, Mexico. *Journal of Geophysical Research*, 109, B04409. <https://doi.org/10.1029/2003JB002843>
- Li, X., Ge, M., Zhang, X., Zhang, Y., Guo, B., Wang, R., et al. (2013). Real-time high-rate co-seismic displacement from ambiguity-fixed precise point positioning: Application to earthquake early warning. *Geophysical Research Letters*, 40, 295–300. <https://doi.org/10.1002/grl.50138>
- Malservisi, R., Schwartz, S. Y., Voss, N., Protti, M., Gonzalez, V., Dixon, T. H., et al. (2015). Multiscale postseismic behavior on a megathrust: The 2012 Nicoya earthquake, Costa Rica. *Geochemistry, Geophysics, Geosystems*, 16, 1848–1864. <https://doi.org/10.1002/2015GC005794>
- McGuire, J. J., & Collins, J. A. (2013). Millimeter-level precision in a seafloor geodesy experiment at the discovery transform fault, East Pacific Rise. *Geochemistry, Geophysics, Geosystems*, 14, 4392–4402. <https://doi.org/10.1002/ggge.20225>
- Meckel, T. A. (2008). An attempt to reconcile subsidence rates determined from various techniques in southern Louisiana. *Quaternary Science Reviews*, 27(15-16), 1517–1522.
- Morton, R. A., Bernier, J. C., & Barras, J. A. (2006). Evidence of regional subsidence and associated interior wetland loss induced by hydrocarbon production, Gulf Coast region, USA. *Environmental Geology*, 50(2), 261.
- Newman, A. V. (2011). Hidden depths. *Nature*, 474(7352), 441–443. <https://doi.org/10.1038/474441a>
- Okada, Y. (1992). Internal deformation due to shear and tensile faults in a half-space. *Bulletin of the Seismological Society of America*, 82, 1018–1040.
- Okaji, M., Yamada, N., & Moriyama, H. (2000). Ultra-precise thermal expansion measurements of ceramic and steel gauge blocks with an interferometric dilatometer. *Metrologia*, 37(2), 165–171.
- Osada, Y., Kido, M., & Fujimoto, H. (2012). A long-term seafloor experiment using an acoustic ranging system: Precise horizontal distance measurements for detection of seafloor crustal deformation. *Ocean Engineering*, 51, 28–33.
- Reilinger, R., McClusky, S., Vernant, P., Lawrence, S., Ergintav, S., Cakmak, R., et al. (2006). GPS constraints on continental deformation in the Africa-Arabia-Eurasia continental collision zone and implications for the dynamics of plate interactions. *Journal of Geophysical Research*, 111, B05411. <https://doi.org/10.1029/2005JB004051>



- Rolandone, F., Nocquet, J. M., Mothes, P. A., Jarrin, P., Vallée, M., Cubas, N., et al. (2018). Areas prone to slow slip events impede earthquake rupture propagation and promote afterslip. *Science Advances*, *4*(1), eaao6596.
- Satake, K. (1994). Mechanism of the 1992 Nicaragua tsunami earthquake. *Geophysical Research Letters*, *21*(23), 2519–2522.
- Sato, M., Ishikawa, T., Ujihara, N., Yoshida, S., Fujita, M., Mochizuki, M., & Asada, A. (2011). Displacement above the hypocenter of the 2011 Tohoku-Oki earthquake. *Science*, *332*(6036), 1395–1395. <https://doi.org/10.1126/science.1207401>
- Segall, P., & Davis, J. L. (1997). GPS applications for geodynamics and earthquake studies. *Annual Review of Earth and Planetary Sciences*, *25*(1), 301–336.
- Spiess, F. N. (1985). Suboceanic geodetic measurements. *IEEE Transactions on Geoscience and Remote Sensing*, *GE-23*(4), 502–510. <https://doi.org/10.1109/TGRS.1985.289441>
- Spiess, F. N., Chadwell, C. D., Hildebrand, J. A., Young, L. E., Purcell, G. H. Jr., & Dragert, H. (1998). Precise GPS/acoustic positioning of seafloor reference points for tectonic studies. *Physics of the Earth and Planetary Interiors*, *108*(2), 101–112.
- Stott, J. K., & Davis, R. A. Jr. (2003). Geologic development and morphodynamics of Egmont Key, Florida. *Marine Geology*, *200*(1-4), 61–76.
- Törnqvist, T. E., Wallace, D. J., Storms, J. E., Wallinga, J., Van Dam, R. L., Blauw, M., et al. (2008). Mississippi Delta subsidence primarily caused by compaction of Holocene strata. *Nature Geoscience*, *1*(3), 173–176.
- Tregoning, P., Watson, C., Ramillien, G., McQueen, H., & Zhang, J. (2009). Detecting hydrologic deformation using GRACE and GPS. *Geophysical Research Letters*, *36*, L15401. <https://doi.org/10.1029/2009GL038718>
- Watson, C., Coleman, R., & Handsworth, R. (2008). Coastal tide gauge calibration: A case study at Macquarie Island using GPS buoy techniques. *Journal of Coastal Research*, *24*(4), 1071–1079.
- Yang, Q., Zhao, W., Dixon, T. H., Amelung, F., Han, W. S., & Li, P. (2015). InSAR monitoring of ground deformation due to CO<sub>2</sub> injection at an enhanced oil recovery site, West Texas. *International Journal of Greenhouse Gas Control*, *41*, 20–28.
- Yokota, Y., Ishikawa, T., Watanabe, S. I., Tashiro, T., & Asada, A. (2016). Seafloor geodetic constraints on interplate coupling of the Nankai Trough megathrust zone. *Nature*, *534*(7607), 374–377. <https://doi.org/10.1038/nature17632>
- Yuill, B., Lavoie, D., & Reed, D. J. (2009). Understanding subsidence processes in coastal Louisiana. *Journal of Coastal Research Special Issue*, *54*, 23–36. <https://doi.org/10.2112/SI54-012.1>
- Zumberge, M. A., Hatfield, W., & Wyatt, F. K. (2018). Measuring seafloor strain with an optical fiber interferometer. *Earth and Space Science*, *5*(8), 371–379.